UCRL-CR-152264
B522033

Investigation of Explosively Driven Fragmentation of Metals-Two-Dimensional Fracture and Fragmentation of Metal Shells: Progress Report II

D. Grady

February 1, 2003

U.S. Department of Energy
Lawrence Livermore National Laboratory

DISCLAIMER

This work was performed under the auspices of the U. S. Department of Energy by the University of California, Lawrence Livermore National Laboratory under Contract No. W-7405-Eng-48.

Investigation of Explosively Driven Fragmentation of Metals — Two-Dimensional Fracture and Fragmentation of Metal Shells

Progress Report II

by
Dennis Grady

Prepared for
University of California
Lawrence Livermore National Laboratory
Livermore, California 94550-94551

February 2003

Contract No. B522033

ARA Project No. 0950

Applied Research Associates, Inc.
4300 San Mateo Blvd. NE, Suite A-220
Albuquerque, New Mexico 87110
(505) 883-3636

Table of Contents

List of Figures

Acknowledgments

The author wishes to acknowledge:

Continuing guidance from Ted Orzekowski, who has maintained the programmatic perspective necessary to focus the theoretical and experimental efforts, and the care and attention to detail of Shannon Moreau in the preparation of the present document.

Section 1 Introduction and Summary

1.1 Background

High explosive enclosed by a metal case qualitatively describes an essential component of high energy systems of importance to the Department of Energy. Detonation of the high explosive causes intense transient pressure loading of the metal following arrival of normal or obliquely incident explosive detonation wave. Subsequent expansion and deformation of the metal case leads to eventual rupture and the opening of fractures and fissures. Details of the rupture process are critical to performance of the system.

Consequently, it is essential that the material and kinematic issues governing the processes of dynamic loading and subsequent failure of an explosive-metal case component within a functioning system be adequately understood. Among the reasons are to quantify existing performance, characterize potential degradation of performance resulting from system aging, and optimizing or maintaining system performance through implementation of structural or material changes.

The physical and engineering issues underlying this dynamic response and failure phenomena are not adequately understood. The purpose of the present program is to identify the key issues and develop theoretical, computational and experimental models needed to achieve a satisfactory theoretical and analysis framework for analysis of metal case failure in the explosive environment.

Specific tasks within the present program include:

1. Models and theories currently being pursued based on physical principles of both the statistical fragmentation concepts of Mott and the energy-based concept of others show promise of providing the analytic and computational methodology capable of predicting explosion-induced fracture and fragmentation of metal components. Experimental studies initiated in the earlier effort offer promise to provide critical test data for validation. The present task shall involve the further refinement and development of the dynamic failure and fragmentation models and theories, and the concomitant application and validation of these models and theories to experimental test data with the focus of providing the analytic methodology sought in the programmatic effort.

2. Stand-alone engineering algorithms and large-scale computer codes will constitute the calculational methodology developed to simulate and analyze the operational system response of metal components in explosive-loading environments. This task will pursue the preparation and implementation of the models and theories of dynamic fragmentation above to the status of engineering and computational analysis tools. The engineering and computer

analysis tools pursued will also be tested against experimental fracture and fragmentation data emerging from the program effort.

1.2 Summary

Two outwardly different theories of the dynamic fragmentation of rapidly expanding metal shells have received sizable attention in recent years. First is the statistics-based theory of Mott (1947) developed in the 1940's. Second is an energy-based theory pursued in the 1980's (Grady et al. 1984; Kipp and Grady 1985). The applicability of both theories to key aspects of the present dynamic fragmentation application is shown here through comparison with the extensive expanding ring fragmentation experiments of Olsen (2001).

The two theoretical approaches are then merged to provide an extended statistical and energy-based theory of fragmentation for the one-dimensional expanding-ring-like fragmentation problem. This extended theoretical development is one of the principal advances achieved within the present reporting period.

Further key advances in the one-dimensional theory include:

1. A general development of the analytic description of the distribution in fragment lengths.

2. A theoretical description and analytic representation of opening separation (crack opening displacement) of fractures during continued expansion following fragmentation.

3. Theoretical clarification of strain to fracture in the one-dimensional fragmentation problem.

4. A statistical characterization accounting for exclusion and impingement associated with the random activation of fractures and the interaction of fracture stress release.

The statistical and energy-based fragmentation theory is extended to the two-dimensional arbitrary expansion and fragmentation of a metal sheet. This extension draws heavily on the fracture and fragmentation relations developed in the one-dimensional theory. Assumptions necessary to the extension are nonetheless sensible and predictions are in reasonable accord with available experimental results.

Specific results include:

1. Analytic predictions of average fragment area and aspect ratio based on the principal in-plane stretching rates and the material fragmentation toughness.

2. Analytic expressions for statistical distributions in fragment area and aspect ratio.

3. Theoretical description of crack opening spacing dependence on in-plane expansion.

A full fragmentation theory of explosively expanding metal shells requires a model for the local strain at fracture onset. In this effort a load maximum failure criterion is explored and extended to the full biaxial extension of an expanding metal sheet. This failure model is not inconsistent with available data. A dependence of the failure model on stress traxiality is not included but could be incorporated later if warranted.

Preliminary engineering models based on the theoretical efforts of this study have also been pursued. The engineering models are written in the framework of a MathCAD mathematical analysis program. Two modeling approaches have been developed:

1. Failure and fragmentation of an expanding metal shell element based on Gurney theory methods in determining the shell loading conditions.

2. Failure and fragmentation of an expanding metal shell element based on the post processing of a computational simulation of the shell loading event.

Application of the engineering models to representative problems is provided. In particular, preliminary comparisons are made with Sandia National Laboratories fragmentation experiments on U6N tubes.

Section 2 Comparisons of Energy-Based and Mott's Statistics-Based Theories of Fragmentation

Two theories appropriate to the dynamic fragmentation of rapidly expanding metal shells have emerged. Both theories have attractive features and demonstrate predictive abilities with available experimental data. As posed, the two theories are based on strikingly different premises and do not, on the surface, appear compatible. The present effort is intended to demonstrate that, with very modest reinterpretation of the initial theoretical premises, the theories do merge providing a richer and more predictive extended theory.

The section starts by outlining both theories as initially presented. Mott's statistics-based theory, as laid out in the early research reports (Mott 1943), and in the later open-literature publication (Mott 1947), is described first. This description also includes analytic representations of the Mott statistical distribution developed later (Grady 1981; Grady 2001). The energy-based theory first discussed by Grady (1980) but, for the present application, more appropriately described in Grady et al. (1984) and Kipp and Grady (1985), is then presented. In both theoretical developments experimental results are described supporting plausibility of the theories.

The section closes with the new theoretical developments which bring Mott's statistical and the energy-based approach together into a broader theory of dynamic fragmentation.

2.1 Mott's Statistics-Based Fragmentation Theory

Three technical reports published within the first half of 1943 reveal the maturing of Mott's understanding of the dynamic fragmentation process and in the last of these reports a statistical theory of fragmentation emerges which is still today the leading theory available. The theory was published several years later in the open literature (Mott 1947). The theoretical development is summarized in the following subsections including analytic extensions of the Mott theory developed by Grady (1981).

2.1.1 The Mott Cylinder

The Mott theory of fragmentation is most readily developed by first introducing the Mott cylinder (or ring) as illustrated in Figure 1. The Mott cylinder is an idealization of an expanding cylindrical shell whose outward motion was imparted by some radial impulse. Mott was personally focused on the natural fragmentation of exploding pipe bombs. The model is certainly applicable to other test conditions such as magnetically driven metal rings. Experiments using the latter expanding ring method will be examined here in evaluating the two fragmentation theories.

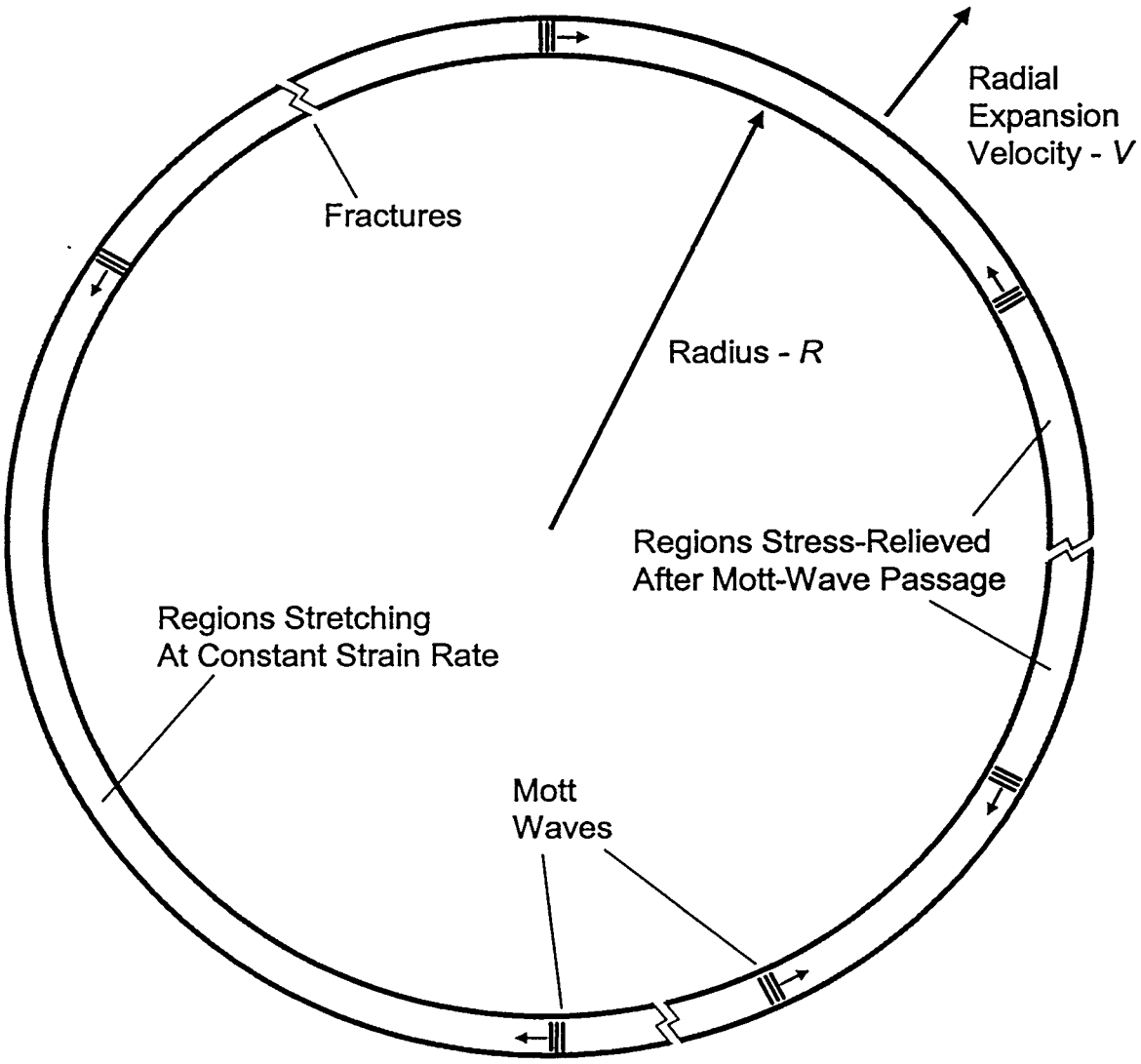

Figure 1. Expanding Mott cylinder illustrating statistical fracture and tension stress release waves.

An explosively-driven expanding metal cylinder is a decidedly multidimensional fragmentation event, and fragmentation of the Mott cylinder is only an approximation to this event. Specifically, the theory attempts to capture the characteristic circumferential spacing of fractures and the statistical distribution in these spacings. It is not intended to account for the axial propagation and interaction of cracks within a finite length cylinder.

Thus, the Mott cylinder is an expanding metal body with radial velocity u and radius r at the time when multiple fracture and breakup of the cylinder proceeds. Just preceding breakup, the cylinder body is in circumferential tension undergoing uniform circumferential stretching at a rate of $\dot{\varepsilon} = u/r$.

Mott proposed that fragmentation proceeded through the random spatial and temporal occurrence of fractures. From sites of fracture, release waves propagate away relieving the tension within the cylinder and precluding the need for further fracture within regions encompassed by tension release waves. Fragmentation is complete when fracture-induced release waves subsume the entire cylinder.

Therefore, within the model for dynamic fragmentation proposed by Mott, two physical issues need to be addressed. First is the issue of when and where fractures occur on the Mott cylinder. Second is the propagation of tensile release waves (Mott waves) away from the sites of fracture. Each will be addressed in turn.

2.1.2 Mott Fracture Activation

Mott put forth arguments that energy dissipation was not of consequence in the fracture process and proposed instead a statistical strain-to-fracture criterion. Mott assumed that fractures occurred at random around the circumference of the cylinder at a frequency governed by a strain dependent hazard function $h(\varepsilon)$ (Hahn and Shapiro 1967) such that $h(\varepsilon)d\varepsilon$ provided the statistical number of fractures occurring within a unit length of the cylinder circumference in the strain interval $d\varepsilon$. It is important to recognize that Mott considered $h(\varepsilon)$ to be an independently measurable property of the material. An alternative and complementary application of the hazard function yields,

$$F_L(\varepsilon) = 1 - e^{-L\int h(\varepsilon)d\varepsilon}, \tag{1}$$

for the cumulative probability of fracture failure in a tensile test of a specimen of length L. Mott in fact used tensile test data on steels to estimate parameters in the function $h(\varepsilon)$ (Mott 1947).

Mott expected $h(\varepsilon)$ to be a strongly increasing function of strain and suggested both an exponential and a power-law function. The former leads to Gumbel statistics while the latter applies to Weibull statistics (Hahn and Shapiro 1967). Mott pursued the exponential hazard function. Here the two-parameter power-law hazard function,

$$h(\varepsilon) = \frac{n}{\sigma}\left(\frac{\varepsilon}{\sigma}\right)^{n-1}, \tag{2}$$

will be used. Analysis suggests little difference in the behavior of the two functional forms. For sensibly large n the parameter σ is the expected value of the strain-to-fracture of a unit length from Equation (1) while σ/n is the standard deviation.

2.1.3 Mott Tension Release

Statistical fracture in the Mott cylinder can now be generally addressed. The functional,

$$F(\varepsilon) = \int_0^{\varepsilon} 2d(\varepsilon - \eta)h(\eta)d\eta, \tag{3}$$

is written. In Equation (3) $h(\eta)d\eta$ is identified as the statistical number of fractures activated on the Mott cylinder at a strain η within interval $d\eta$. The function $d(\varepsilon - \eta)$ is the distance traveled by a tensile stress release wave over the strain interval $\varepsilon - \eta$. (Since strain rate is assumed to be constant over the duration of the fracture process, strain and time are synonymous through $\varepsilon = \dot{\varepsilon}t$.)

In Equation (3) $F(\varepsilon)$ is readily seen to provide the fraction of the Mott cylinder which has been encompassed by stress release waves emanating from sites of fracture at a current strain ε. The equation also determines the fraction of the cylinder in which further fracture is precluded. A form of Equation (3) was derived by Mott in the original 1943 reports.

An inspection of Equation (3) reveals that the function $F(\varepsilon)$ will exceed unity at sufficiently large strain. This non-physical result is a consequence of not accounting for two factors in the fracture activation and stress wave propagation process. First, the fracture activation function $h(\varepsilon)$ does not exclude the activation of further fractures within regions previously stress relieved. Second, the stress release function $d(\varepsilon)$ does not account for the impingement and the overlap of opposing release waves from separate neighboring fractures. Thus Equation (3) is only sensible for a dilute number of fractures early in the fracture and release process.

To account for fracture exclusion and wave impingement in the statistically random Mott model, a statistical method introduced by Johnson and Mehl (1939) will be used (Grady 1981). Random exclusion and impingement is accounted for through the relation,

$$D(\varepsilon) = 1 - e^{-F(\varepsilon)}, \tag{4}$$

providing the fraction of the Mott cylinder encompassed by fracture stress release waves at any strain ε. The function $D(\varepsilon)$ does approach unity as ε becomes large.

2.1.4 Fracture Stress Release Function

Functional form of the stress release function $d(\varepsilon)$ has not been specified. There are several possibilities. If the expanding Mott cylinder is elastic at the time of fracture then a constant elastic release wave velocity governed by the elastic modulus is sensible. Mott, however, considered an expanding ductile metal cylinder and assumed a material on the tensile yield surface governed by a constant flow stress Y. Instantaneous fracture and rigid-ideally-plastic constitutive response leads to the stress release function (Mott 1947; Grady 2001),

$$d(\varepsilon) = \sqrt{\frac{2Y}{\rho\dot{\varepsilon}^2}\varepsilon} \tag{5}$$

where $\varepsilon = \dot{\varepsilon}t$.

2.1.5 Fracture Number Prediction

Given explicit forms for the fracture activation function in Equation (2) and the stress release function in Equation (5), statistical predictions of the number of fracture (and fragments) produced in the breakup of the Mott cylinder can be obtained. Accounting for the stress relieved fraction of the cylinder $D(\varepsilon)$ the number of fractures at a strain ε is given by,

$$N(\varepsilon) = \int_0^{\varepsilon} (1 - D(\eta))h(\eta)d\eta \,. \tag{6}$$

Completing the integral in Equation (3) to first obtain $D(\varepsilon)$ through Equation (4), integration of Equation (6) to infinite strain yields [Grady, 2001],

$$N = \beta_n \left(\frac{\rho\dot{\varepsilon}^2}{2\pi Y}\frac{n}{\sigma}\right)^{n/(2n+1)}, \tag{7}$$

for the number of fractures per unit length, where,

$$\beta_n = \left(\frac{2}{2n+1}\frac{\Gamma(n+1/2)}{\Gamma(n)}\right)^{2n/(2n-1)} \Gamma\left(\frac{2n}{2n+1}\right). \tag{8}$$

For reasonably large n the constant β_n approaches one and the power approached one-half leading to a linear dependence on the expansion strain rate. The fracture number is determined by the standard deviation σ/n of the power-law fracture frequency function $h(\varepsilon)$ as was noted by Mott (1947).

The temporal history of fractures appearing on the Mott cylinder can be determined by retaining the strain dependence of the integral in Equation (6).

The random placement of fractures on the Mott cylinder both in space and in time as assumed in the Mott model allows for calculation of the statistical distribution of fracture spacing (fragment lengths). This calculation was performed graphically by Mott (1947) and has been completed by analytic methods (Grady 1981; Grady 2001) only for the special case of $n=1$ in the power-law fracture frequency function. The calculated analytic distribution in fracture spacing by this analytic method is,

$$f(x)=\frac{\beta^2}{4}\frac{1}{x_o}\left(\frac{x}{x_o}\right)^3 e^{-\frac{1}{4}(x/x_o)^3}\int_o^1\left(1-y^2\right)e^{-\frac{3}{4}(x/x_o)^3y^2}dy, \qquad (9)$$

where $\beta=3\Gamma(2/3)$ and $x_o=(3\sigma Y/2\rho\dot{\varepsilon}^2)^{1/3}$. The sensitivity of the distribution to the functional form of the fracture frequency function $h(\varepsilon)$ is not known but comparison of the analytic distribution from Equation (9) and the graphic distribution determined by Mott (1947) suggests that this sensitivity is probably small. Both the analytic and the graphical distribution are compared in Figure 2. In summary, the statistics-based theory of dynamic fragmentation developed in the seminal study of Mott provides a physically plausible and intellectually satisfying description of the fragmentation process. Within the one-dimensional model of the Mott cylinder the theory is fully predictive, providing the average fragment size and the distribution about the average, as well as the statistical temporal history of fracture and the strain-to-fracture. Comparisons of the Mott theory with experimental data will be considered shortly.

2.2 Energy-Based Fragmentation Theory

A theory of dynamic fragmentation based on starkly different initial assumptions has been pursued by Grady et al. (1984), and Kipp and Grady (1985). Again, one-dimensional fracture and fragmentation on the Mott cylinder provides the model for development of the theory. The fundamental difference in the two theories is that Mott assumed energy dissipated in the fracture process was not of concern and that fracture at a site on the cylinder would be effectively instantaneous. In contrast, energy dissipation and an associated fracture delay time lies at the heart of the energy-based fragmentation theory.

2.2.1 The Fracture Calculation

Formulation of the energy-based fragmentation theory on the expanding ductile Mott cylinder proceeds by extending the analysis developed by Mott to calculate the time history of release waves (Mott waves) emanating from sites of fracture. The extension of the analysis proceeds by considering, rather than instantaneous fracture, a fracture resistance which reduces from the flow stress Y to zero as a crack-opening-displacement parameter y goes from zero to some critical crack opening displacement y_c. An assumption of linear reduction of the fracture resistance leads then to a fracture energy dissipation $\Gamma=Yy_c/2$. The treatment is quite analogous to the crack-

opening-displacement models of Dougdale (1960) and Barrenblatt (1962) in consideration of quasistatic fracture resistance. Momentum balance for the rigid ideally plastic problem leads to the following differential expression for the position x of the Mott release wave (Kipp and Grady 1985),

$$\rho\dot{\varepsilon}x\frac{dx}{dt}=\frac{Y^2}{2\Gamma}y, \tag{10}$$

while motion of the crack opening displacement gives,

$$\frac{dy}{dt}=\dot{\varepsilon}x, \tag{11}$$

The coupled equations are readily solved yielding,

$$x(t)=\frac{1}{12}\frac{Y^2}{\rho\Gamma}t^2, \tag{12}$$

for the motion of the Mott release wave while the crack opening displacement over $0 \le y \le y_c$ is given by,

$$y(t)=\frac{1}{36}\frac{\dot{\varepsilon}Y^2}{\rho\Gamma}t^3. \tag{13}$$

The time to fracture is determined by the time for the crack opening displacement to achieve y_c and is calculated to be,

$$t_c=\left(\frac{72\rho\Gamma^2}{Y^3\dot{\varepsilon}}\right)^{1/3}. \tag{14}$$

Over the time t_c the Mott release wave travels a distance from the site of fracture,

$$x_c=\left(\frac{3\Gamma}{\rho\dot{\varepsilon}^2}\right)^{1/3}. \tag{15}$$

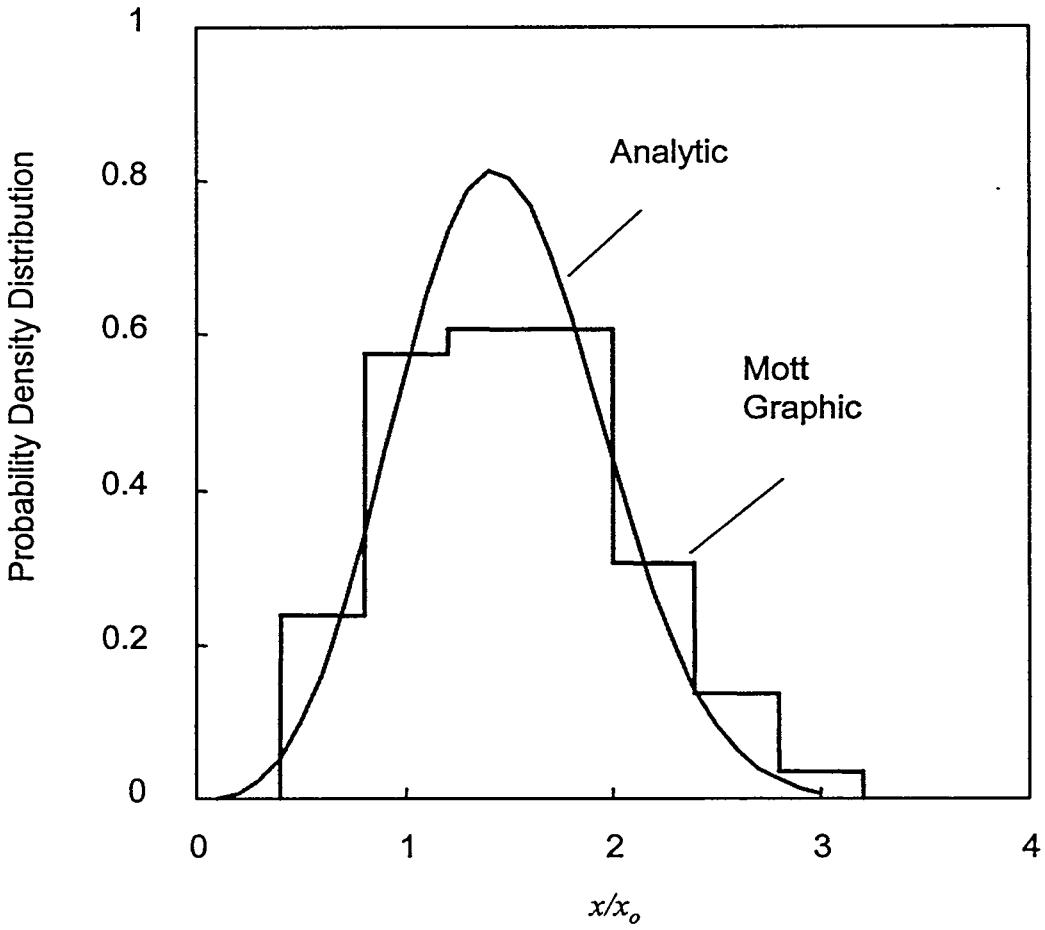

Figure 2. Comparison of the graphic and the analytic solution for the Mott distribution of fragment lengths.

2.2.2 Fragment Size and Fragmentation Toughness

The distance x_c propagated by the Mott release wave determines the minimum spacing of separate fractures permitting fracture completion without interaction of release waves. The theory assumes that the nominal fragment length is given by twice the distance x_c or,

$$x_o = \left(\frac{24\Gamma}{\rho\dot{\varepsilon}^2}\right)^{1/3} . \tag{16}$$

The fracture resistance Γ is considered to be a property of the material characterizing the dissipation in the fracture growth process. It is possible under certain failure modes to estimate the fracture resistance Γ from other material properties [e.g. Kipp and Grady, 1985; Grady, 1993]. Fracture toughness is the property commonly used to characterize the static (and dynamic) fracture properties of metals. Thus, it is sensible in the present development to define a property with the dimensions of fracture toughness through the relation of linear elastic fracture mechanics relating fracture strain energy release and fracture toughness. Namely,

$$K_f = \sqrt{2E\Gamma} , \tag{17}$$

where E is the elastic modulus. The property K_f will be identified as the fragmentation toughness of the metal and will not presume any relationship to the clearly defined static fracture toughness.

The expression for the characteristic fracture spacing from Equation (16) then becomes,

$$x_o = \left(\frac{\sqrt{12}K_f}{\rho c\dot{\varepsilon}}\right)^{2/3} . \tag{18}$$

The energy-based theory does not address the issue of the statistical distribution of fragment sizes. It is assumed that Equation (18) provides an average fragment size and that the fragment number per unit length is provided by the inverse of Equation (18), or,

$$N = \left(\frac{\rho c\dot{\varepsilon}}{\sqrt{12}K_f}\right)^{2/3} . \tag{19}$$

Equation (19) provides the energy-based spatial fracture frequency prediction to be compared with Equation (7) of the Mott statistical theory.

2.3 Comparisons With Experiment

2.3.1 Experimental Fragmentation Studies

A range of diverse experimental fragmentation investigations could be used, and in fact has been used, to explore the predictive abilities of Mott's statistics-based theory and the more recent energy-based fragmentation theory. Here consideration will be restricted to a recent quite thorough study of dynamic fragmentation of magnetically driven uranium 6% niobium (U6N) metal rings (Olsen 2001). The experimental geometry nicely replicates the fragmentation model assumed by Mott and provides data directly comparable with the theoretical predictions.

In this work U6N metal rings approximately 30 mm in diameter and with a 0.75-mm square cross section were accelerated by a pulsed magnetic field to radial velocities of 50–300 m/s. Actual acceleration is provided by an aluminum pusher ring which accommodates most of the induced electric current. The aluminum ring is arrested prior to fragmentation allowing free flight of the U6N ring preceding breakup.

Radial velocity history of the U6N rings was measured with time-resolved velocity interferometery or VISAR (Barker and Hollenbach 1972). Measured deceleration of the freely expanding ring prior to fragmentation was used to calculate a tensile flow stress of nominally 1 GPa. Fragmentation occurred at an expansion of about 30%.

In each test the number of fragments produced (equivalently, the number of fractures) was determined. Fragment number versus the expansion velocity of fragmentation are shown for the series of U6N expanding ring experiment in Figure 3. The anomalous point high on the graph is the consequence of one test on an overaged U6N sample. A least squares fit, excluding the one anomalous point, provided the power law representation of the data shown in Figure 3. In one representative test each fragment was separately weighed and the cumulative fragment size distribution shown in Figure 4 was obtained.

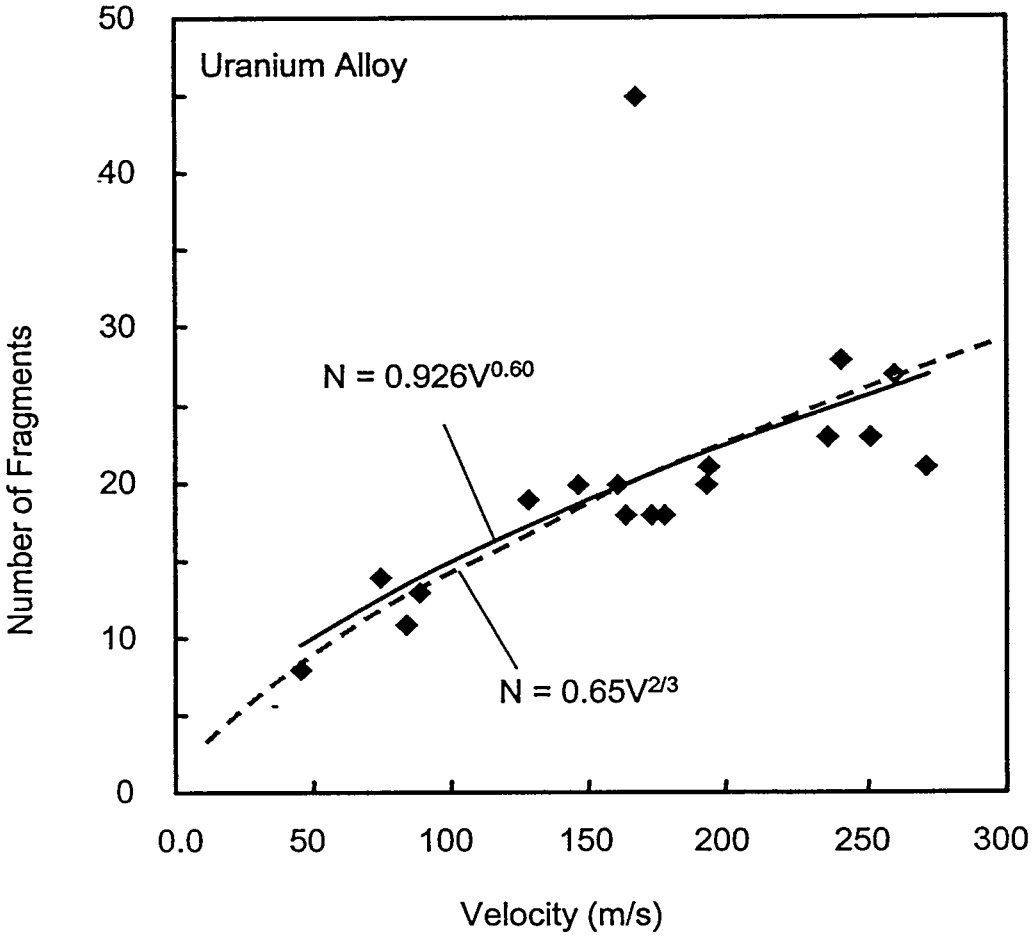

Figure 3. Fragment number versus expansion velocity at fracture for U6N expanding ring fragmentation tests.

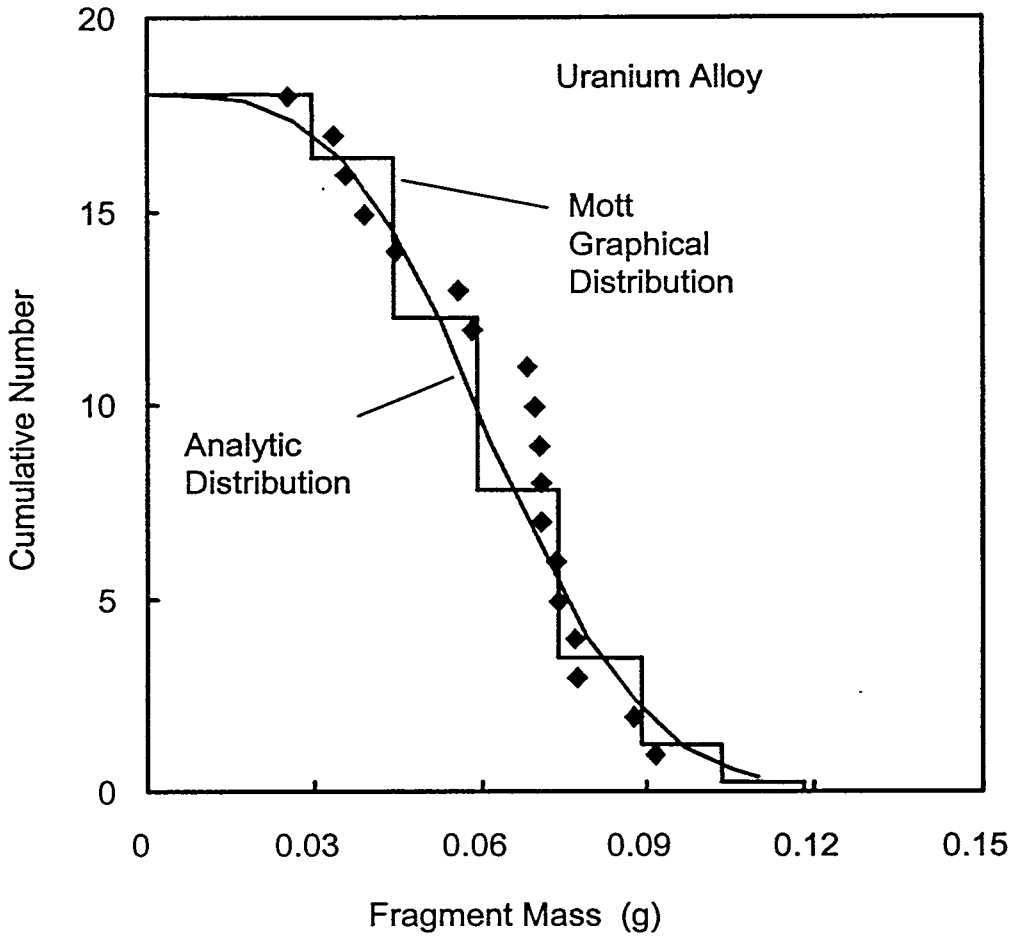

Figure 4. Comparison of cumulative fragment distribution for one representative U6N expanding ring fragmentation tests with theoretical Mott fragment size distribution.

2.3.2 Comparisons with the Mott Statistics-Based Theory

Weibull parameters σ and n necessary to predictions of the fragment number and dependence on velocity are not available for the U6N material tested. Hence only sensibility of the experimental results can be examined. The observed power law dependence of fragment number on expansion velocity close to two-thirds indicates that the Weibull parameter n in Equation (7) is very close to unity. Assuming $n=1$, the second Weibull parameter is calculated to be $\sigma = 7.7\times10^{-5}/\mathrm{m}$. The standard deviation in strain to fracture calculated from Equation (1) is σ/L. Considering specimens of length of order of one centimeter, the nominal length of fragments in the ring tests, a scatter in strain to fracture of approximately 10^{-2} or about 3% of the observed 0.30 strain to fracture is calculated. Thus Weibull parameters within the Mott statistical theory for the fragmentation of U6N rings are plausible.

Prediction of the distribution in fracture spacing is also a facet of Mott's statistical theory. Comparison of both the graphic distribution generated by Mott and the analytic distribution from Equation (9) both displayed in Figure 2 are compared with the distribution determined experimentally in Figure 4. The observed distribution and the theoretical distributions based on the Mott statistical fracture theory are in reasonable accord.

2.3.3 Comparisons with the Energy-Based Theory

The energy-based fragmentation theory directly predicts from Equation (19) a two-thirds power dependence of fragment number on strain rate or, equivalently, the expansion velocity at fracture. A two-thirds power dependence curve is compared with the data and the experimental fit in Figure 3 and shows sensible agreement with the data.

To further test the energy-based theory the fragmentation toughness is calculated through Equation (19) for each experiment. This representation is shown in Figure 5. A value of K_f in excess of 60 $\mathrm{MPa}\cdot\mathrm{m}^{1/2}$ determined from the fragmentation data is remarkably close to a static fracture toughness of approximately $90-110$ $\mathrm{MPa}\cdot\mathrm{m}^{1/2}$ measured on similar U6N alloys.

Other features observed in the U6N ring fragmentation experiments also attest to the importance of energy dissipation and finite fracture time in the dynamic fracture process. Inspection of fragments revealed fully developed necking regions—a signature of fractures which were enveloped with tensile release (Mott) waves and fracture growth arrested before full fracture and separation was achieved.

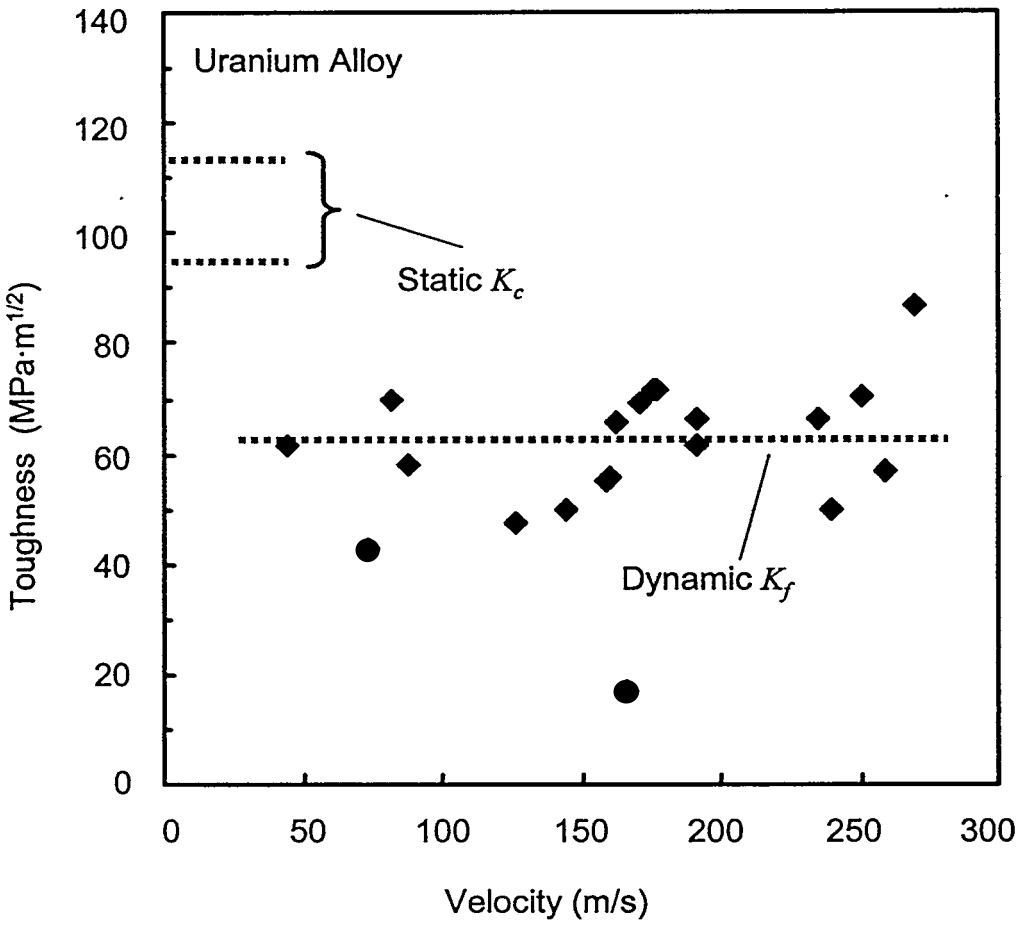

Figure 5. Dynamic fragmentation toughness calculated through theoretical relation relating fragment number, expansion rate and material toughness.

2.4 A Statistical and Energy-Based Theory of Fragmentation

Clearly both Mott's statistical theory and the energy-based theory have features in accord with the results of the U6N expanding ring fragmentation experiments. Frequency, and in particular, statistical spacing, of fractures are consistent with predictions of the Mott theory. The favorable strain rate dependence and the very close agreement between static fracture toughness and the inferred dynamic toughness are, on the other hand, well predicted by the energy-based theory. It would seem that a broader theory encompassing concepts from both the statistics-based and the energy-based approaches is warranted.

2.4.1 A Merging of Theories

The statistical fragmentation theory of Mott is based on two functional properties characterizing response of the material in a dynamic fragmentation event. First is a strain-dependent fracture activation function $h(\varepsilon)$ which has been selected here of the power law form,

$$h(\varepsilon) = \frac{n}{\sigma}\left(\frac{\varepsilon}{\sigma}\right)^{n-1}. \tag{20}$$

Second is the diffusion-governed tensile release propagation function from sites of fracture,

$$d(\varepsilon) = \sqrt{\frac{2Y}{\rho\dot{\varepsilon}^2}}\varepsilon. \tag{21}$$

Together the Mott theory yields the spatial fracture frequency from Equation (7),

$$N = \beta_n\left(\frac{\rho\dot{\varepsilon}^2}{2\pi Y}\frac{n}{\sigma}\right)^{n/(2n+1)}. \tag{22}$$

In contrast, the energy-based theory yields for the same spatial fracture frequency,

$$N = \left(\frac{\rho\dot{\varepsilon}^2}{24\Gamma}\right)^{1/3}. \tag{23}$$

The theories are equivalent if the Weibull constants have the unique values,

$$n = 1, \tag{24}$$

and,

$$\sigma = \beta_1^3\frac{12}{\pi}\frac{\Gamma}{Y} \cong 5\frac{\Gamma}{Y}. \tag{25}$$

Thus, the requisites of the energy theory would uniquely constrain the Weibull parameters and the functional form of the fracture activation function of Mott's statistical theory. Equation (25) identifies a material-specific length scale σ and requires, through Equation (20), that the fracture activation function be constrained to a constant $h(\varepsilon) = h_o = \sigma^{-1}$.

The fracture activation statistical hazard function as was proposed by Mott (Equation (20)) and as constrained by the energy theory are illustrated in Figure 6. The function $h(\varepsilon)$ specifies fracture activation frequency as increasing plastic strain ε is achieved. Thus, increasing expansion rates are required to achieve increasing levels of strain to fracture.

Below the strain at which the two functions cross in Figure 6, the lower rate of fracture activation is provided by the rapidly increasing power-law expression for $h(\varepsilon)$. Above the strain the constant expression for $h(\varepsilon)$ inferred from energy considerations provides the lesser rate of fracture activation.

From the Mott statistical development outlined earlier the cumulative strain to fracture is calculated from the expression,

$$\varepsilon_f = \int_0^\infty (1 - D(h))d\eta . \tag{26}$$

It is readily shown that the cumulative strain to fracture, $\varepsilon_f = \alpha_n \dot{\varepsilon}^{2/(2n+1)}$, where α_n is a constant function of the material properties, increases with expansion rate $\dot{\varepsilon}$.

Thus, the comparison indicates that, with increasing expansion rate, a strain to fracture which exceeds the cross-over strain is eventually achieved. Fragmentation and the frequency of fracture become governed by fracture energy dissipation properties.

This observation suggests a reinterpretation of the fracture activation functions. The rapidly increasing Mott function would, more appropriately, be the fracture seeding function. This function characterizes the perturbations and defects in the body leading to fracture (the seeds of fracture) but does not necessarily specify the fracture activation process itself. Above the cross-over strain the constant energy-based function provides the fracture survival rate. Below the cross-over strain in the fracture seeding function limits the fracture activation and there is a one-to-one correspondence between fractures seeded and fractures activated. Above the cross-over strain, however, many fractures are initiated but energy requirements limit fracture survival and only a subset of fractures seeded achieve activation.

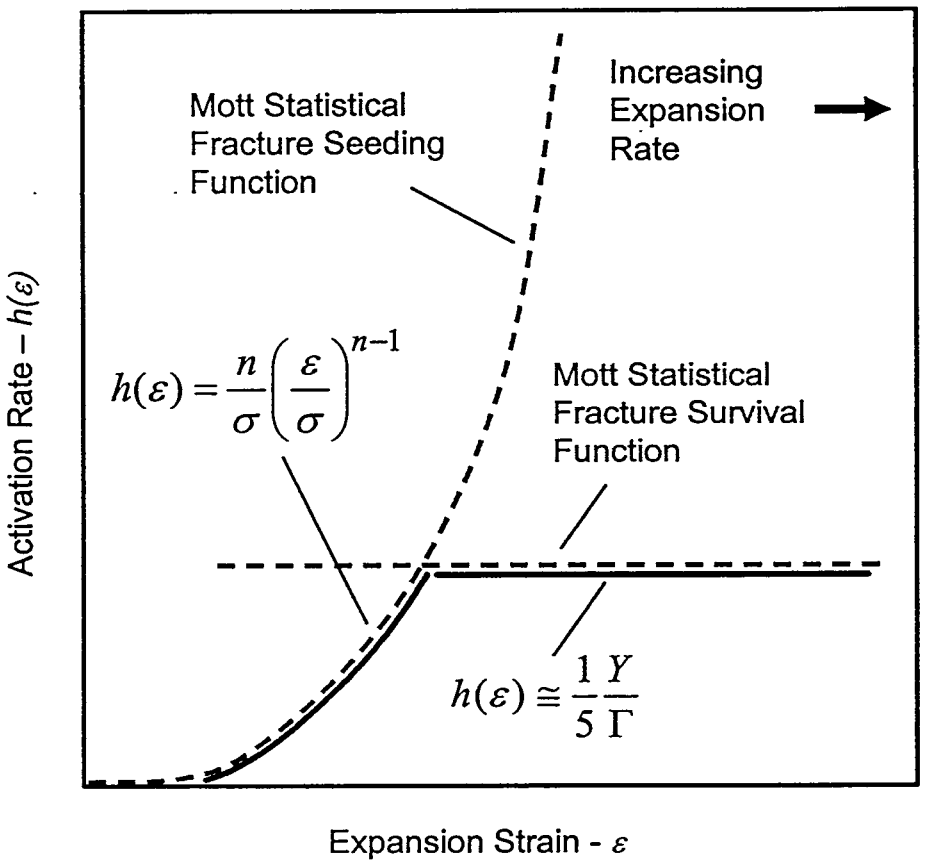

Figure 6. Graphical interpretation of fracture functions in the merging of Mott statistics-based and energy-based fragmentation theories.

2.4.2 Strain to Fracture

In the statistical theory of Mott both strain to fracture and fracture frequency are uniquely determined through the parameters σ and n in the power-law fracture activation function. The theory of Mott, however, cannot also account for the two-thirds power dependence of the average fragment number on strain rate predicted by the energy-based theory, and also observed in the U6N expanding ring experiments.

With the extended statistical energy-based theory, strain to fracture in addition to the statistical fragment size and strain-rate dependence features can be accounted for. Prediction is dependent on proper selection of the Mott fracture seeding function,

$$h(\varepsilon) = \frac{n}{\sigma}\left(\frac{\varepsilon}{\sigma}\right)^{n-1}, \tag{27}$$

and the energy governed fracture survival function,

$$h(\varepsilon) = h_o \cong \frac{1}{5}\frac{\Gamma}{Y}, \tag{28}$$

where h_o is provided by Equation (25). The cumulative number $n(\varepsilon)$, or rate of fracture seeding and fracture survival functions (the integral of Equation (27) and Equation (28) are plotted in Figure 7 (compare with Figure 6)).

The new parameter revealed in Figure 7 is the constant of integration ε_o of the fracture survival function. The Mott fracture activation function is determined by the solid segments of both functions. The theory has acquired an additional material parameter but now supports the prediction of strain to fracture in addition to statistical fracture frequency and spacing distribution. At fracture strain rates into the energy-governed fragmentation regime it is readily shown that the statistical strain to fracture from Equation (26) is,

$$\varepsilon_f = \varepsilon_o + \alpha_1 \varepsilon^{2/3}, \tag{29}$$

where α_1 is calculated through Equation (26) from the energy-based Mott fracture properties.

This broader interpretation of fragmentation merges both the statistical principals of Mott and the fracture energy requirements of the energy-based theory. A wider set of properties characterizing the solid body of interests is required, however. The Mott seeding function characterizes the defect state of the body governing the strain-dependent nucleation of potential fractures. Weibull parameters in the two-parameter power law function serve this purpose in the present development. The Mott survival function incorporates the energy dissipation, or fragmentation toughness, properties of the material. Further material properties and supporting theory are needed to establish the strain to fracture onset.

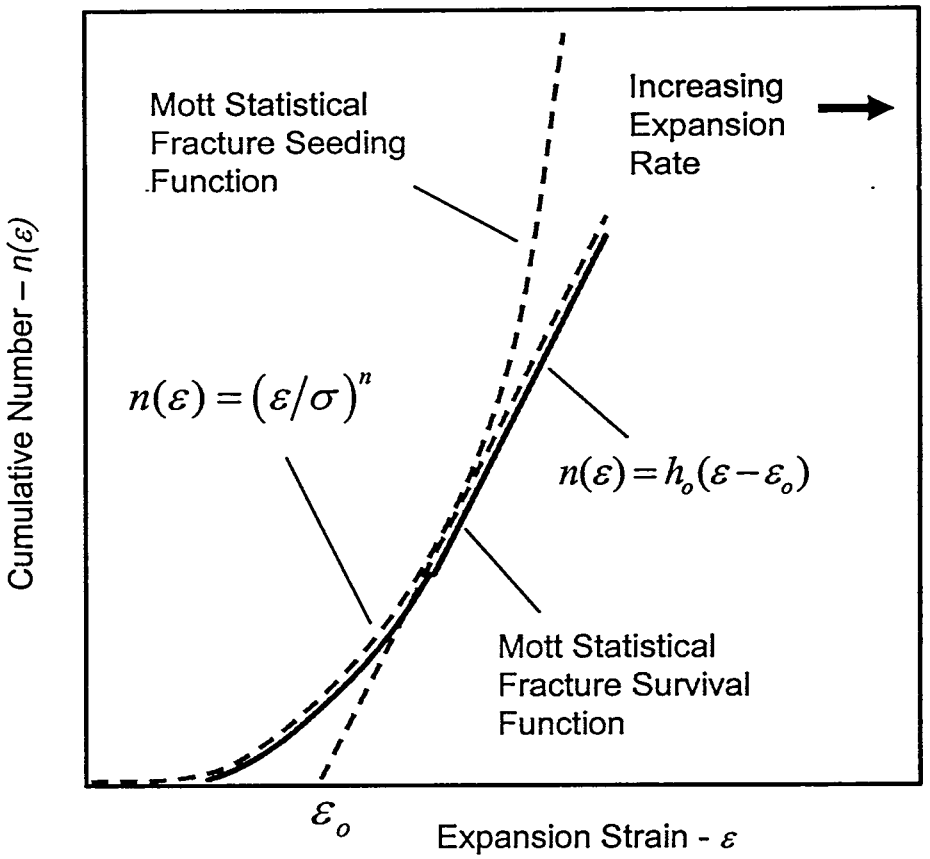

Figure 7. Cumulative fracture seeding and survival functions in statistical energy-based theory of fragmentation.

2.4.3 Supporting Calculations

Partial support for the extended theory is provided by a one-dimensional computational simulation of the Mott fragmentation process performed by Kipp and Grady (1986). At that time it was recognized that interplay between dynamics of the fragmentation event and the population of flaws seeding the multiple fracture process could lead to conditions in which flaw structure controlled the extent of fragmentation on one hand while energy limitations controlled fragmentation on the other. A rationale for analytically merging the range of behaviors was not recognized, however.

The following computer simulations of dynamic fragmentation were performed to support experimental fragmenting ring studies performed at that time (Grady et al. 1984). A one-dimensional finite difference wave code was used to calculate the response of an aluminum rod or wire 0.1 m in length stretching plastically at a flow stress $Y = 100$ MPa and at a uniform stretching rate $\dot{\varepsilon} = 10^4/\text{s}$. Fracture sites were introduced randomly in time according to a constant nucleation rate parameter $h(\varepsilon) = h_o$ and randomly positioned within the length of the rod. The nucleation rate h_o was the only parameter varied over the series of calculations. When fracture was nucleated at a computational cell, stress in that cell was relaxed from the flow stress Y to zero as the cell distended such that plastic fracture energy within that cell of $\Gamma = 2 \times 10^4$ J/m^2 was dissipated. The number of fragments produced as the nucleation rate h_o was varied over approximately one order of magnitude was determined from the simulations and are shown in Figure 8. Although not directly duplicating the conditions of Figure 6, the relationship is apparent.

At reduced nucleation rates every fracture nucleation site grows to full fracture. The number of fractures and the corresponding characteristic fragment size is thus governed fully by the flaw structure and the fracture nucleation (seeding) function. As the nucleation rate is increased the number of nucleated fracture sites which fail to grow to completion correspondingly increases. At the highest nucleation rates the number of fragments becomes independent of the number of fracture sites nucleated and is determined strictly by the fracture energy Γ resisting fracture growth. The energy governed constant fracture survival rate, $h_o \cong Y\dot{\varepsilon}/5\Gamma$, identified in Figure 8, is sensibly consistent with the expected transition from flaw limited to energy-limited fragmentation.

A cumulative fragment length distribution from one computational simulation is compared with the predicted graphic and analytic Mott distribution from Figure 2 in Figure 9. The computational distribution is fully consistent with the statistical theory.

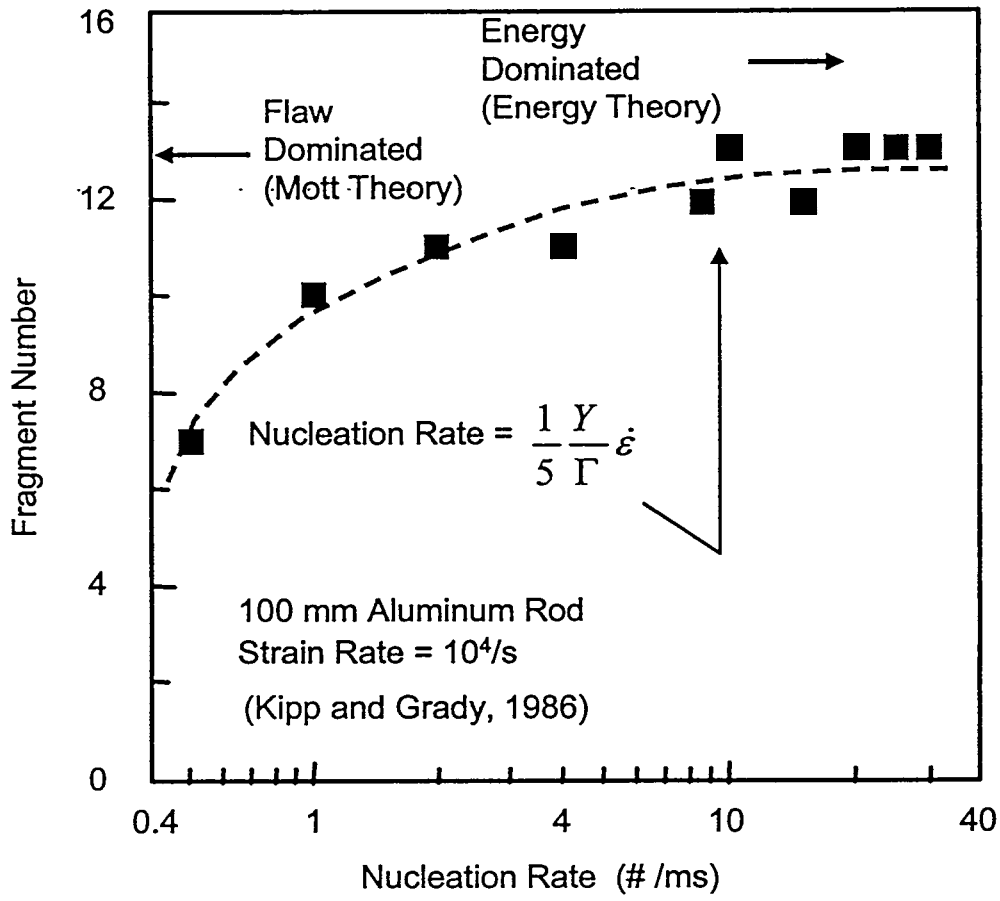

Figure 8. Fragment number from computational simulations.

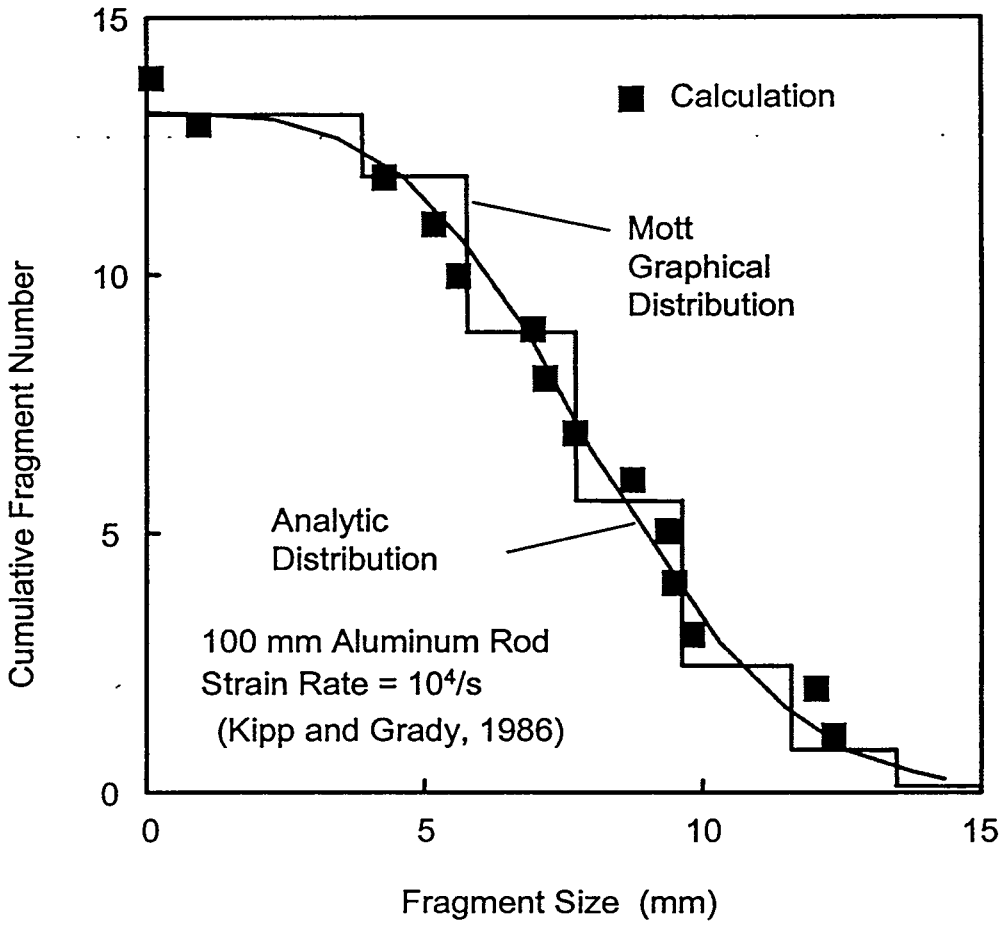

Figure 9. Fragment distribution from computational simulation and comparisons with Mott statistical fragmentation theory.

2.4.4 The Fracture Physics

Of the properties required to characterize the response of the expanding metal cylinder, the fracture energy captured through the property Γ is probably the most apparent. That some degree of work must be expended, and some fracture energy overcome, in opening the cracks delineating the fragment boundaries produced in the fragmentation event is inherently reasonable. Less apparent are details of the deformation mechanisms occurring in the fracture growth and dissipation process. Plastic necking, adiabatic shearing and ductile fracture are all viable mechanisms. It is likely that all of the above mentioned mechanisms will contribute to some degree.

Considerably less intuitive are the material features responsible for onset of fracture; analytically expressed in this development by the Mott seeding function and quantified by the Weibull parameters in the power-law hazard function. In most events leading to the dynamic expansion and fragmentation of ductile metal rings and shells a degree of stable plastic stretching is accommodated before fracture occurs. This deformation is most likely a consequence of stabilizing plastic hardening of the component metal. As plastic hardening saturates, however, continued stretching and thinning becomes inherently unstable and susceptible to perturbations in the deformation. Sources of these perturbations are far from certain. Granularity of the device metal is a reasonable source of deformation perturbations. Perturbations from metal granularity leading to fracture would suggest sensitivity of the fragmentation process (particularly the effective strain to fracture) to grain size and related material issues.

There are also convincing indications that surface features, either inherent or induced, play a role in the perturbations seeding fracture onset. Imperfections in metal-explosive interfaces leading to deformation perturbation as detonation-induced shock waves are coupled into the metal system must also be considered.

2.5 Further Theory and Analysis

In this section some final theoretical issues are addressed before moving on to the two-dimensional fragmentation of an expanding surface. First, the statistical treatment of the interaction of multiple fractures was not treated in the original work of Mott (1947). This part of the theory has application to both the one- and two-dimensional fragmentation problem and is considered in further detail in this section. The analytic determination of statistical fragment size distributions from the statistical theory has been performed for specific Mott fracture activation and growth laws. This development involves analytic details which are not readily transparent. Here, a more general development of the size distribution relations is developed which provides a clearer outline of the procedures. Lastly, after completion of fracture, continued expansion of the fragments results in statistical distribution of opening cracks and the associated crack-opening displacement. An analysis is presented which provides an analytic statistical description of the crack opening displacement for the one-dimensional expanding Mott cylinder.

2.5.1 The Statistical Interaction of Fractures

The statistical approach to the treatment of the interaction of fractures in the dynamic fragmentation of a body was outlined in an earlier section. In the present section the issue is discussed further and expanded on.

The activation and subsequent stress release of fractures initiated as a consequence of the tensile stretching of a ductile metal shell is illustrated schematically in Figure 10. The Mott cylinder considered previously illustrates the uniform expansion and one-dimensional (circumferential) fracture of a ring or cylinder. The biaxially stretching surface, on the other hand, depicts the two-dimensional (in-plane) fracture of the expanding surface.

In the Mott statistical theory of fragmentation a function $h(\varepsilon)$ characterizes the rate of activation of fractures in the unruptured stretching plastic body. It is a material property which characterizes the initial or evolving defect structure of the material including interior and/or surface features. In energy-limited fragmentation $h(\varepsilon)$ accounts for the fracture toughness or shear band energy which must be overcome to initiate a fracture. The material function $h(\varepsilon)$ cannot, however, account for the interaction of multiple fractures through stress relief (Mott) waves. The interaction of activated fractures and associated stress release regions is not explicitly treated in the theory.

Similarly, the stress release growth function $d(\varepsilon)$, which determines the distance or domain of the stress release region as a function of continued expansion or stretching ε after fracture activation, is developed from the physics of wave propagation after a single fracture has occurred at some point. It does not account for the behavior when the stress-release zones from two nearby fractures begin to interact.

Thus early in the fracture process when the number of fractures and associated release domains are sufficiently dilute such that the rate of fracture activation is sufficiently well represented by $h(\varepsilon)$, and such that interactions between neighboring release zones are negligible, then the fraction of the region stress relieved by fracture is readily calculated from,

$$F(\varepsilon) = \int_0^{\varepsilon} d(\varepsilon - \eta) h(\eta) d\eta \ . \tag{30}$$

The fracture activation law does not exclude attempts to activate fractures within previously stress-relieved regions, for instance, as illustrated in Figure 11.

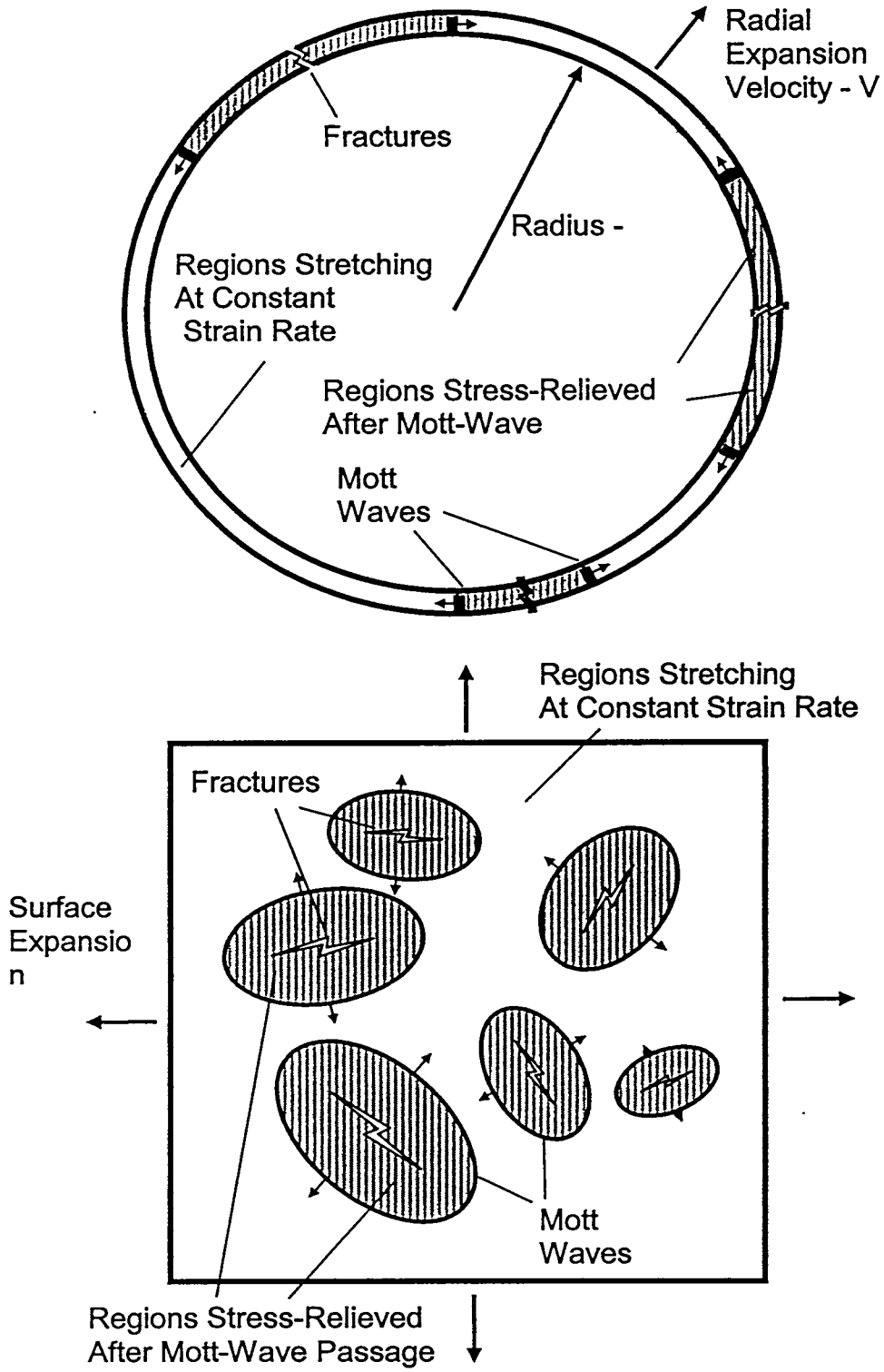

Figure 10. Illustrates activation and subsequent stress release of multiple fractures in the dynamic expansion of ductile metal shells for the Mott cylinder (upper) and a biaxially expanding sheet.

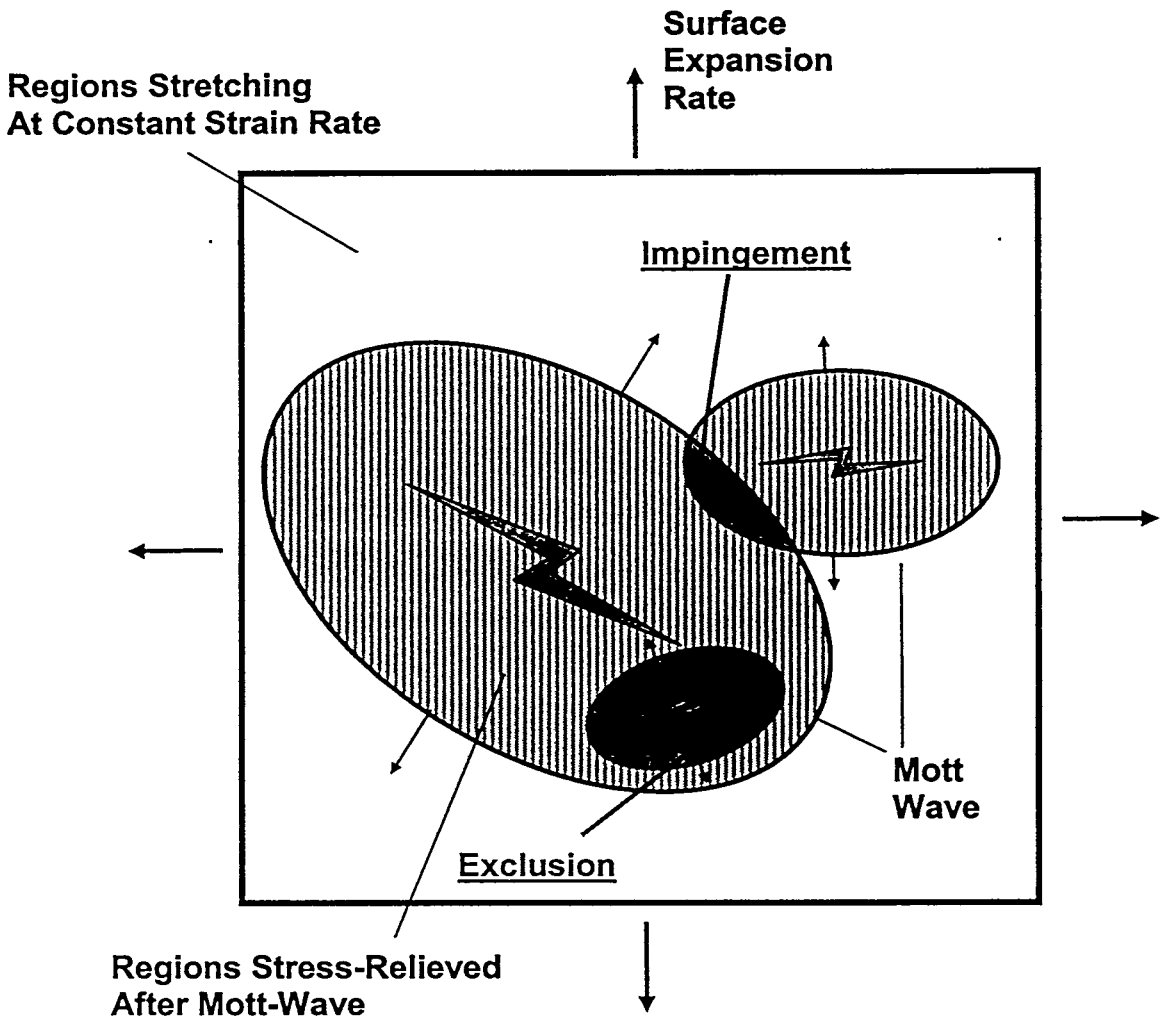

Figure 11. Illustrates fracture activation exclusion and release wave impingement which must be accounted for in the statistical fragmentation theory.

A seminal study in the statistical theory of accounting for exclusion and impingement in kinetic processes of materials was put forth by Johnson and Mehl (1939). The essential idea is illustrated in Figure 12 in which random size circles of area dA_{xi} are placed at random on a region of unit size. The total projected area of i circles placed on the region is then the sum,

$$A_x = \sum_i dA_{xi} \ . \tag{31}$$

The actual area covered by the circles (the area fraction due to the unit size of the region), because of overlap of the circles, is the union of the i circles,

$$A = \bigcup_i dA_{xi} \ , \tag{32}$$

such that $A < A_x$. In the random placement of an additional circle of area dA_x, as shown in the Figure, the probability of any element of that circle falling outside of the area A is,

$$P(A) = 1 - A \ . \tag{33}$$

Consequently, the change in area A is just,

$$dA = P(A)dA_x = (1 - A)dA_x \ , \tag{34}$$

which integrates to,

$$A = 1 - e^{-A_x} \ . \tag{35}$$

The statistical process for dealing with extinction and impingement in kinetic processes was interpreted by Getis and Jackson (1971) in another way. In Figure 13 circles placed at random on the region are assumed to come from a distribution of circles with expected value in radius of $E(r^2)$. The projected fraction is then,

$$A_x = \pi E(r^2) n \ , \tag{36}$$

where n is the average number of circle centers per unit area of the region. Random placement of the circle centers is a Poisson point process in which case the probability of k circles covering a particular point in the region is,

$$P(k) = \frac{A_x^{\,k} e^{-A_x}}{k!} \ . \tag{37}$$

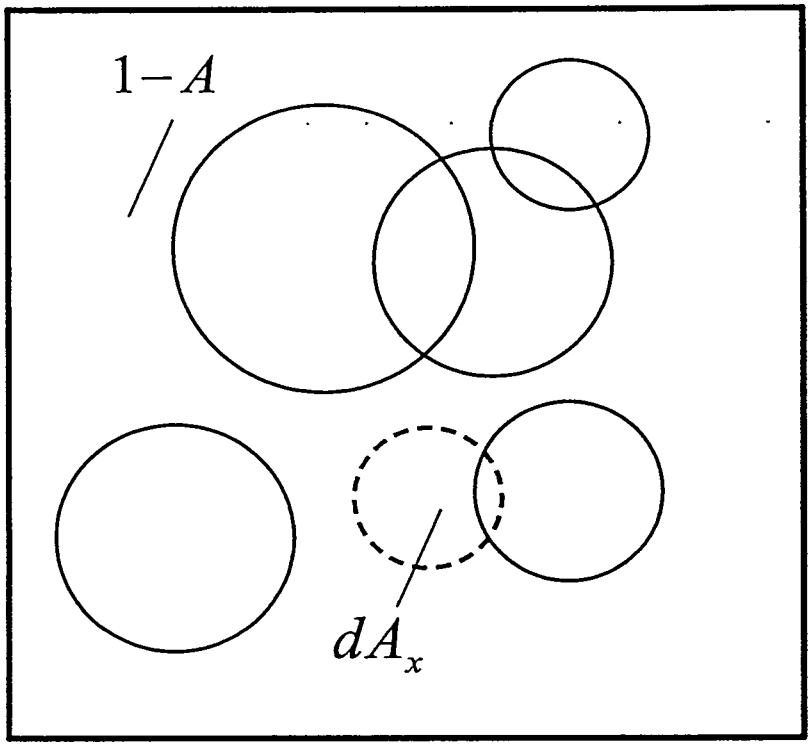

Figure 12. The random placement of overlapping circles illustrates the statistical model accounting for exclusion and impingement developed by Johnson and Mehl (1939).

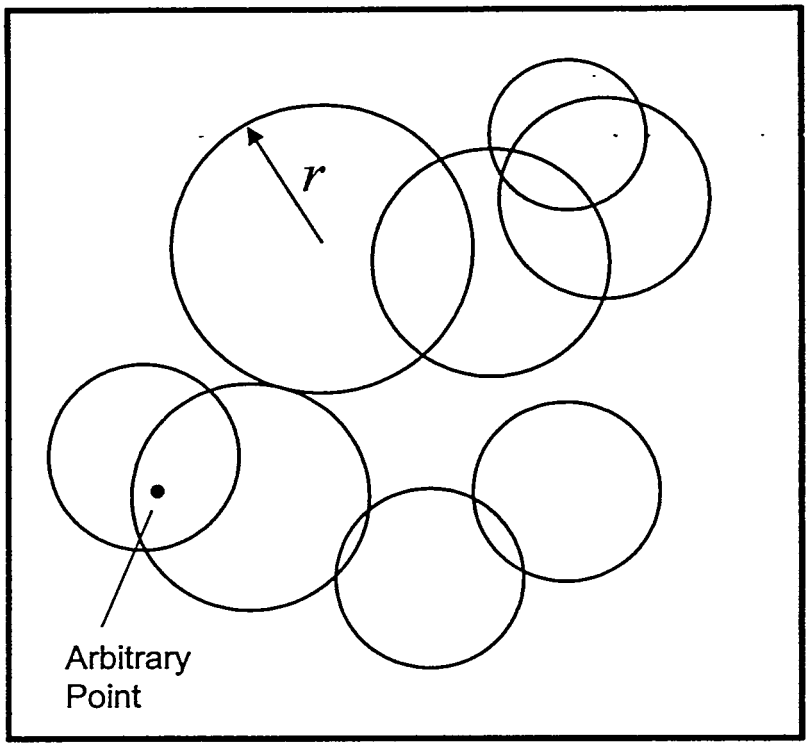

Figure 13. The Getis and Jackson (1971) statistical model proceeds from the Poisson probability of random circles covering an arbitrary point multiple times.

The fraction of the region covered is then,

$$A = P(k \geq 1) = 1 - P(k = 0) \ , \tag{38}$$

or,

$$A = 1 - e^{-A_x} \ , \tag{39}$$

equivalent to the derivation of Johnson and Mehl (1939).

This statistical theory is used to account for the exclusion of fracture activation and the impingement of stress release regions in the present development of the Mott fragmentation theory and accordingly the area fraction of stress release regions at any expansion ε is,

$$D = 1 - e^{-F(\varepsilon)} \ , \tag{40}$$

where $F(\varepsilon)$ is provided by Equation (30).

Application of the Johnson-Mehl or the Getis-Jackson statistical model to the Mott theory of the fragmentation of rapidly expanding ductile shells seems appropriate. The statistical model is particularly appropriate within the context of the Mott fragmentation model for the propagation of Mott stress release waves which excludes communication of signals of any type to regions ahead of the release waves. In application within metals with both elastic and plastic hardening properties applicability could probably be questioned. The approach is nonetheless physically attractive, leads to tractable analytic solutions for a number of features of the fracture process, and can be experimentally tested.

2.5.2 The Development of Size Distribution in the Mott Theory

The Mott fragmentation theory, when combined with the statistical treatment of extinction and impingement, leads to continuous analytic predictions of feature of the fracture process such as number of fractures, fracture spacing, and cumulative strain, along with the time dependence of these features through the fracture process. A remarkable product of this theory is analytic relations for the statistical distributions for fragment size in the fragmentation event. Here we focus on the one-dimensional fragmentation event in which fragment size is unambiguously determined by the fragment length. An approach for determining size distributions in the two-dimensional fragmentation of an expanding area is pursued in the next section. These distribution relations for one-dimensional fragmentation were derived previously for several specific fracture activation and stress release growth laws. We here wish to develop the size distribution relation in general terms. This development, when not buried in the algebra of a specific analysis, provides insight into the workings of the theoretical model.

First, the number density of fractures at any time, or strain ($\varepsilon = \dot{\varepsilon} t$), during the fracture process is given by,

$$N(\varepsilon) = \int_0^{\varepsilon} (1 - D(\eta)) h(\eta) d\eta = \int_0^{\varepsilon} e^{-F(\eta)} h(\eta) d\eta \ . \tag{41}$$

This fracture number relation is appropriate for one-dimensional fracture on the circumference of the Mott cylinder as well as two-dimensional fracture of the expanding surface.

As previously noted, fracture on the Mott cylinder (ring) uniquely characterizes the size of fragments. Namely, they are the arc lengths of the regions between fractures. Random fracture activation on the surface, however, does not uniquely constrain fragment dimensions. Further assumptions concerning the extension and intersection of fractures are necessary before assessment of statistical fragment size can be accomplished. From here on focus is strictly on the one-dimensional fragmentation problem.

When a fracture occurs at a point on the Mott cylinder two Mott release waves are created and propagate away from the fracture as illustrated in Figure 14. Therefore, ignoring exclusion and impingement, the number of Mott waves activated at strain ε is,

$$N(\varepsilon) = 2 \int_0^{\varepsilon} h(\eta) d\eta \ . \tag{42}$$

To account for the collision and arrest of active Mott waves as illustrated in the figure, and to account for attempted activation within zones of stress release, Equation (42) is multiplied by the exclusion and impingement factor $(1 - D)$,

$$N(\varepsilon) = 2(1 - D(\varepsilon)) \int_0^{\varepsilon} h(\eta) d\eta = 2e^{-F(\varepsilon)} \int_0^{\varepsilon} h(\eta) d\eta \ , \tag{43}$$

providing the number of active Mott waves at any strain ε. The rate of change of $N(\varepsilon)$ is then,

$$\frac{dN(\varepsilon)}{d\varepsilon} = 2e^{-F(\varepsilon)} h(\varepsilon) - N(\varepsilon) F'(\varepsilon) \ , \tag{44}$$

which will be written as,

$$\frac{dN(\varepsilon)}{d\varepsilon} = I^{+}(\varepsilon) - N(\varepsilon) I^{-}(\varepsilon) \ . \tag{45}$$

The rate of activation of Mott waves is provided by $I^{+}(\varepsilon)$ while the fraction of active Mott waves arrested at strain ε is given by $I^{-}(\varepsilon)$.

The effort now will focus on determining the number of Mott waves which activated at some earlier strain η and arrested at later strain ε. These waves will have all

propagated the same distance determined by the release domain growth law $d(\varepsilon-\eta)$. Therefore, let,

$$\delta N_o = I^+(\eta)\delta\eta \ , \tag{46}$$

specify the number of Mott waves activated at earlier strain η within increment $\delta\eta$. Further, let δN be the number of the original δN_o surviving at strain $\varepsilon > \eta$. Then the number arrested at strain ε within increment $d\varepsilon$ is just,

$$d(\delta N) = -\delta N I^-(\varepsilon)d\varepsilon \ . \tag{47}$$

Equations (44) and (45) provide $I^-(\varepsilon) = F'(\varepsilon)$ and Equation (47) integrates to,

$$\delta N = Ce^{-F(\varepsilon)} \ . \tag{48}$$

The constant of integration C is determined from the requirement $\delta N = \delta N_o$ at $\varepsilon = \eta$ and provides,

$$\delta N = I^+(\eta)e^{F(\eta)-F(\varepsilon)}\delta\eta \ . \tag{49}$$

Substituting from Equation (47) finally yields,

$$d^2N = I^+(\eta)I^-(\varepsilon)e^{F(\eta)-F(\varepsilon)}d\eta d\varepsilon \ , \tag{50}$$

for the number of Mott waves activated at strain η and arrested at strain ε.

The change of integration variables,

$$u = \varepsilon + \eta \ , \qquad v = \varepsilon - \eta \ , \tag{51}$$

and integration over u provides,

$$p(x) \propto \int_{u=\varepsilon+\eta} I^+(\eta)I^-(\varepsilon)e^{F(\eta)-F(\varepsilon)}d\eta d\varepsilon \ , \tag{52}$$

where $x = d(\varepsilon-\eta)$ is the distance of Mott wave propagation from activation to arrest and $p(x)$ is the statistical distribution in Mott propagation distances.

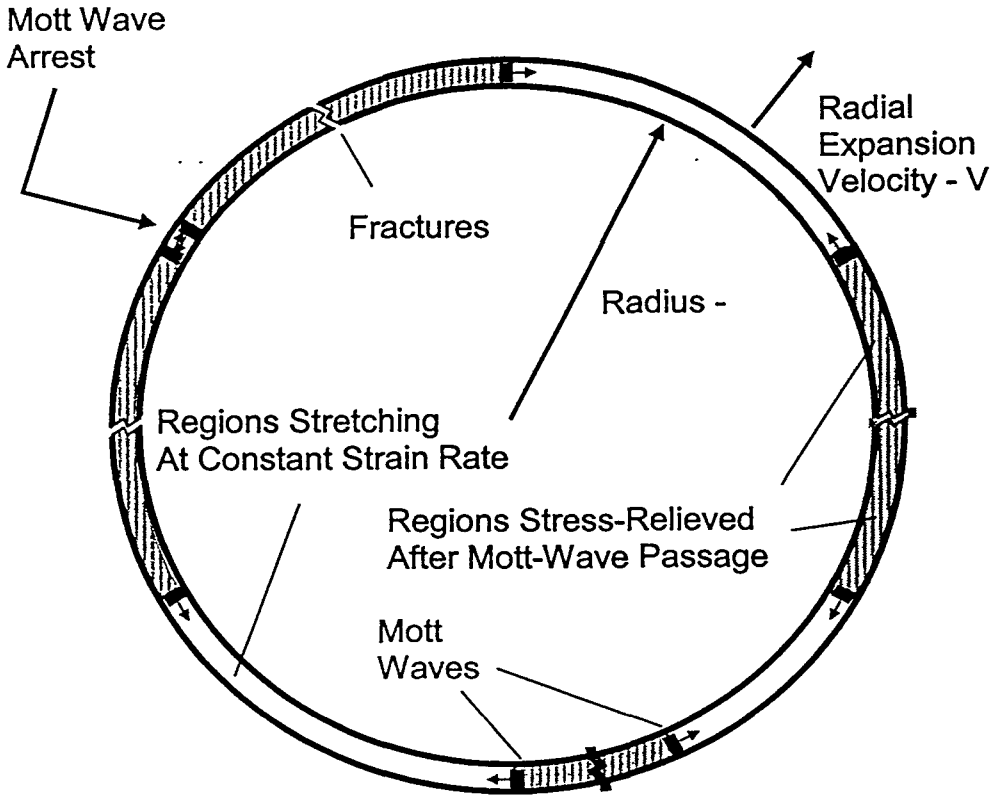

Figure 14. Activation and arrest of Mott stress release waves from points of fracture.

Equation (52) does not, however, provide the distribution in fragment size. As shown in Figure 15, Mott wave propagation distances combine in pairs to determine the length of a fragment. Thus the analytic expression for the statistical distribution in fragment lengths is,

$$f(x) = \int_{\xi = x_1 - x_2} p(x_1) p(x_2) dx_1 dx_2 \ , \tag{53}$$

where $p(x_1)$ and $p(x_2)$ are the distributions provided in Equation (52) and the change of variables,

$$x = x_1 + x_2 \ , \qquad \xi = x_1 - x_2 \ , \tag{54}$$

complete the integration in Equation (53).

For the special Mott problem in which the activation rate $h(\varepsilon) = h_o$, a constant, and Mott wave propagate according to $d(\varepsilon) = \sqrt{2Y\varepsilon / \rho\dot{\varepsilon}^2}$, Equation (53) provides the distribution,

$$f(x) = \frac{\beta^2}{4} \frac{1}{x_o} \left(\frac{x}{x_o} \right)^3 e^{-\frac{1}{4}(x/x_o)^3} \int_o^1 \left(1 - y^2\right) e^{-\frac{3}{4}(x/x_o)^3 y^2} dy \ , \tag{55}$$

presented earlier.

2.5.3 Distribution in Crack-Opening Displacement

The expanding Mott cylinder undergoes multiple dynamic fractures which is statistically random in both the position of occurrence and the time of the fractures. Following fracture, the ring segments continue to expand outward and the crack-opening displacement at the points of fracture that separate the segments continues growing to accommodate the expansion and separation of the individual outwardly directed fragments. The dimension of the gaps between segments (the crack-opening displacement) and the statistical spread in the dimensions of these gaps at any time after fracture are the subject of the discussion and analysis in this section.

The dynamics in the neighborhood of a single fracture are illustrated in Figure 16 and Figure 17. In Figure 16 the conditions of a uniform velocity gradient corresponding to the stretching rate $\dot{\varepsilon}$ prior to fracture activation is depicted by the dashed line. After fracture Mott waves propagate away from the fracture separating regions in front of the waves and flowing plastically at stretching rate $\dot{\varepsilon}$, from rigid regions behind the waves moving at uniform velocity. The velocity profile at some time t after fracture is illustrated by the solid line in Figure 16.

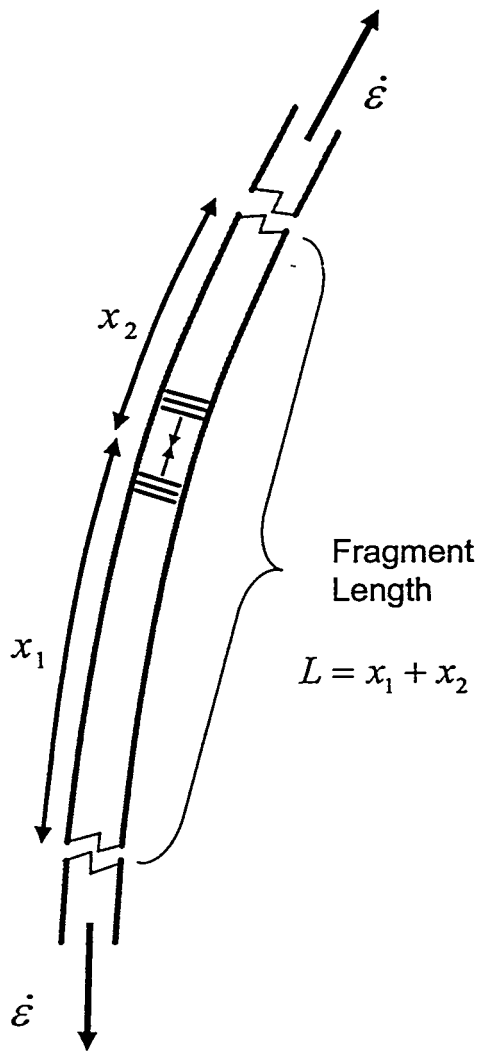

Figure 15. Mott propagation distances combine in pairs to determine fragment lengths.

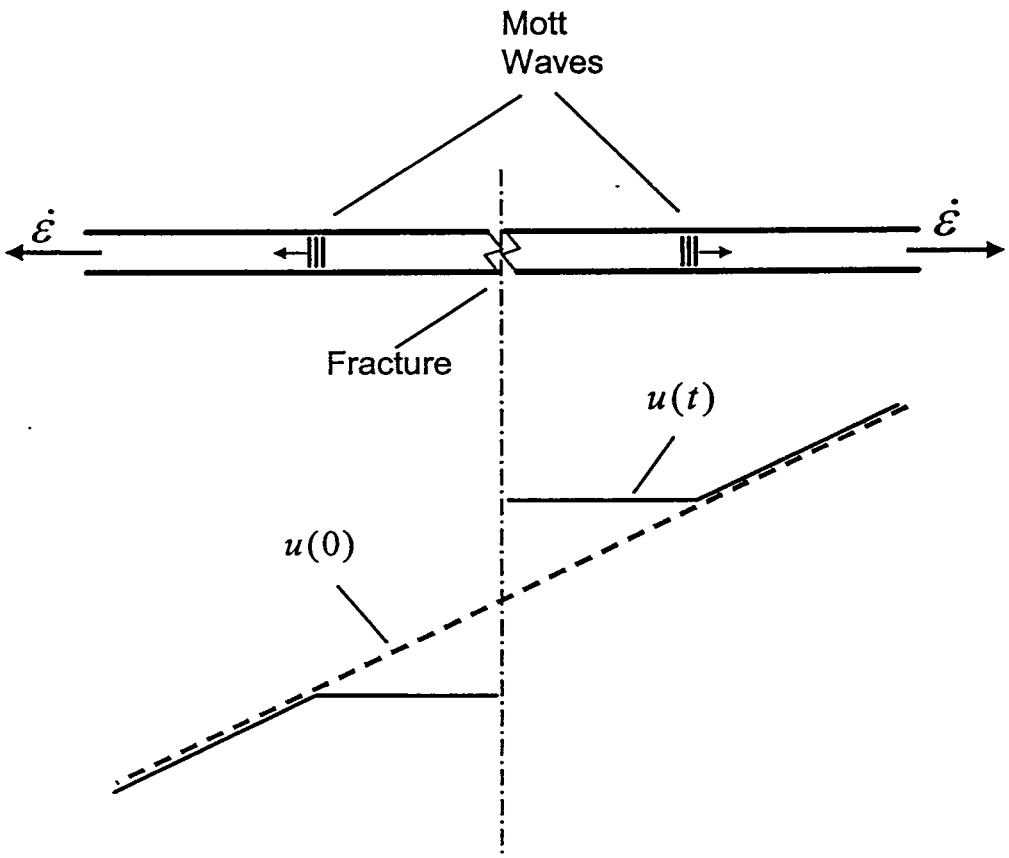

Figure 16. Velocity profile in the stretching ring following fracture and determined by the Mott rigid-plastic wave solution.

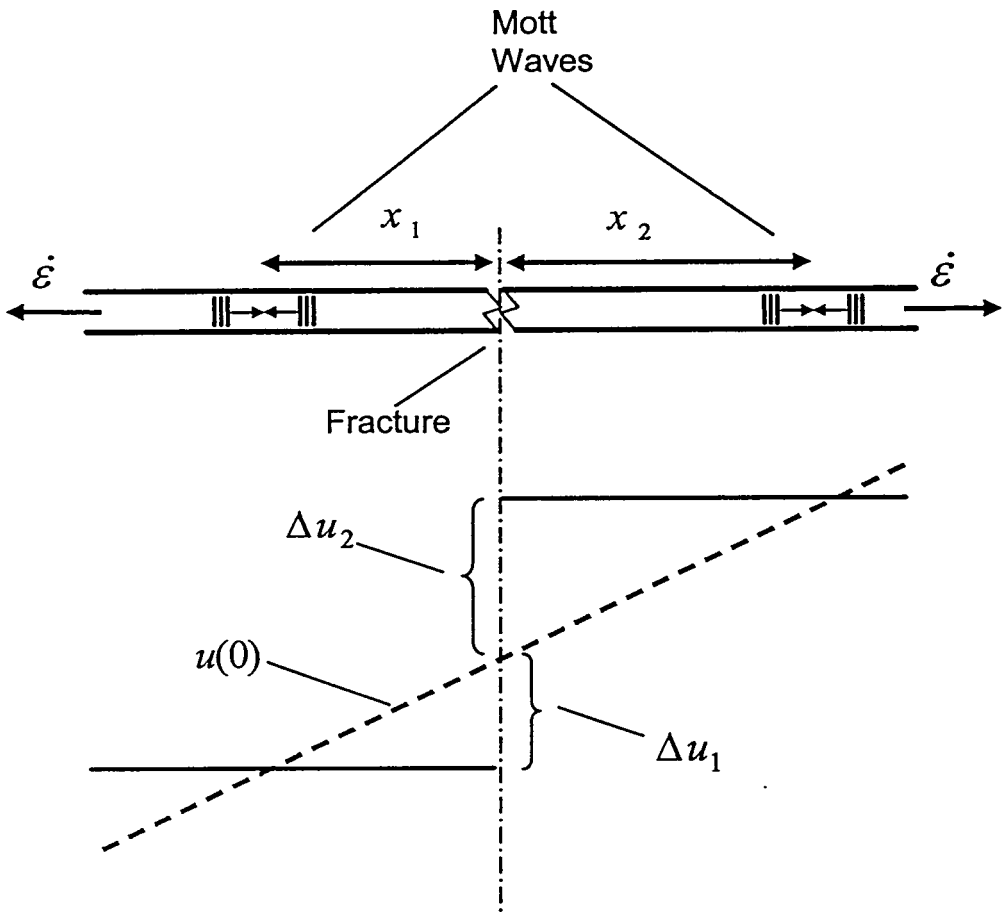

Figure 17. Differential velocity of ring segments adjacent to fracture following completion of wave interaction.

Opposing Mott waves are activated at neighboring fractures to the right and to the left of the fracture depicted in the figures. The collision of two opposing Mott waves from adjacent fractures concludes velocity gradients and plastic flow within the intervening mass segment. This segment continues to move at a constant velocity equal to the velocity at the position of the collision point of the Mott waves.

The segment to the left of the fracture moves away from the position of the initial fracture at a velocity $\Delta u_1 = x_1\dot{\varepsilon}$ while that to the right at a velocity $\Delta u_2 = x_2\dot{\varepsilon}$ where x_1 and x_2 are the distances between the fracture point and the respective Mott wave collision points, as shown in Figure 17. The crack-opening displacement is then,

$$w(t) = (x_1 + x_2)\dot{\varepsilon}t \ , \tag{56}$$

where t is the time after fracture.

There is a characteristic time t_c over which the statistical fracture process and interaction of propagating Mott waves proceeds. This characteristic time was derived from the Mott wave solution and provided by Equation (14). The time after fracture in Equation (56) is assumed to be sensibly larger than t_c.

At any time t there will be a statistical spread $g(w)$ in the crack-opening displacement w provided by Equation (56). This comes about because the distances of stress release x_1 and x_2 determined by the propagation distances of Mott waves emanating from the fractures are themselves random. These same distances, when interpreted as the propagation distances between two adjacent fractures, determine the length of the intervening fragment segment, and uniquely determine the statistical distribution in fragment lengths for the one-dimensional Mott fragmentation problem as developed previously (Equation (9) and Equation (55)). Although the distances x_1 and x_2 governing the crack-opening displacement in Equation (56) are on opposite sides of the fracture, the statistical development of $g(w)$ is equivalent. Consequently the distribution $g(w)$, shown in Figure 18, and the fragment length distribution $f(x)$ from Equation (9) are related according to,

$$g(w)dw = f(x)dx \ , \tag{57}$$

or,

$$g(w) = f(x(w))\frac{dx}{dw} \ . \tag{58}$$

The characteristic crack-opening displacement at time t is $w_o(t) = x_o\dot{\varepsilon}t$ where x_o from the derivation of Equation (9) is $x_o = (3\sigma Y / 2\rho\dot{\varepsilon}^2)^{1/3}$. Or, with the expression for $\sigma \cong 5\Gamma / Y$ from Equation (25), $x_o \cong (5\Gamma / 2\rho\dot{\varepsilon}^2)^{1/3}$.

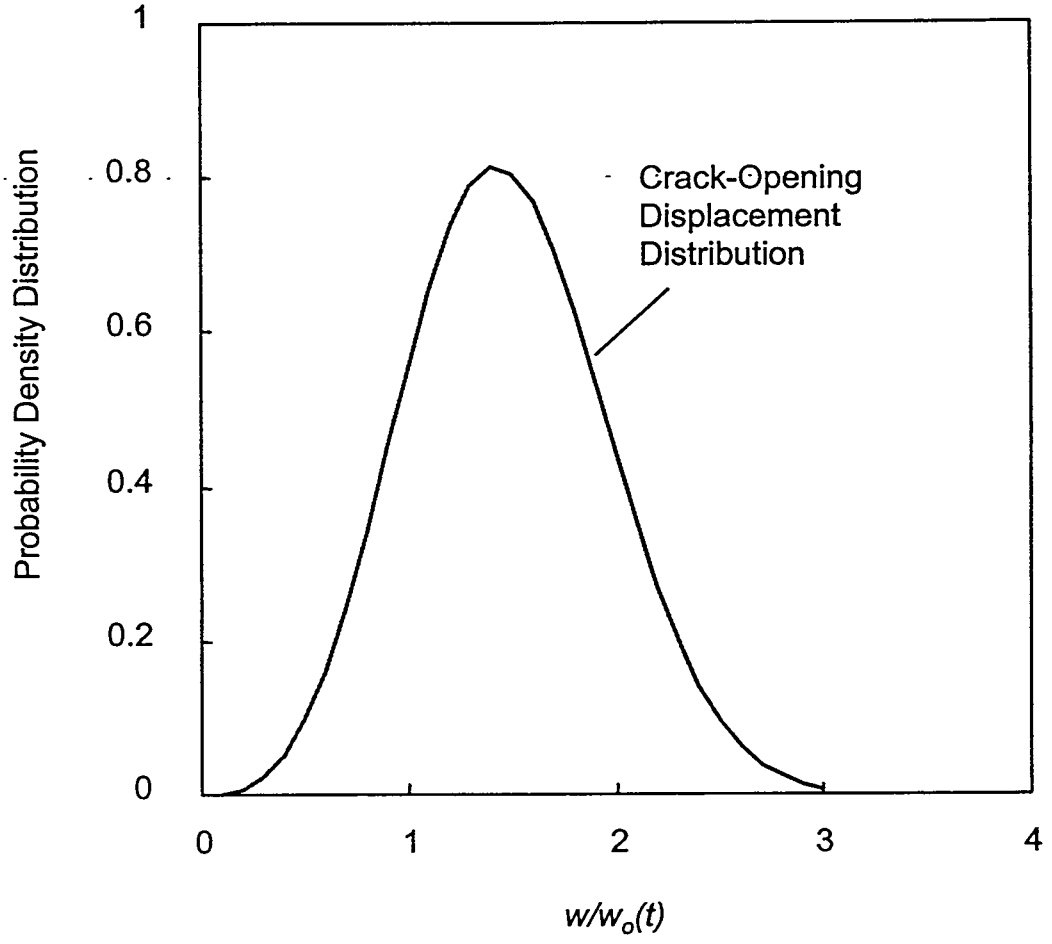

Figure 18. Distribution in crack-opening displacement. Displacement is normalized by characteristic crack-opening displacement $d_o(t)$.

The distribution in crack-opening displacement is shown in Figure 18. Displacement is normalized by the characteristic crack-opening displacement $w_o(t) = x_o \dot{\varepsilon} t$. Thus, fragment lengths and crack-opening displacement exhibit the same distribution in spread about the mean. Also the distribution in crack-opening does not depend on the time after fracture.

Section 3 Extension to Expanding Surface Fragmentation

Development of a statistical energy-based theory of fragmentation of stretching ductile metals has been restricted to one-dimensional geometries such as expanding rings or, at best, a uniformly expanding cylinder where the theory is intended to describe the average and statistical spacing of axial fractures. In this section a theory will be pursued to describe the breakup of a biaxial expanding shell or membrane of ductile metal in which stretching rates in mutually orthogonal directions are each nonzero and are, in general, different. A specific case of interest, of course, is that of a stretching spherical shell segment in which the orthogonal stretching rates are the same.

3.1 Fracture Independence in Mutually Orthogonal Directions

In the development of the present two-dimensional fragmentation theory it will be assumed that at a point on the surface of the expanding body orthogonal principal stretching directions can be determined and that fracture in the two principle directions are independent and governed by the conditions of the linear fragmentation theory developed in the earlier sections. This approach is illustrated in Figure 19, where principal stretching directions on a surface are identified and a corresponding statistical distribution of fractures along the x and the y stretching directions partition the surface into a statistical distribution of fragment areas.

3.2 Fragment Size and Aspect Scales

Within the energy governed region of the linear statistical fragmentation theory a fracture activation rate, and a corresponding fracture spacing length scale, was determined based on a property of the material identified as the fragmentation toughness and the rate of stretching leading to fracture. The same relation will be used to determine the fracture spacing length scale in both orthogonal principal stretching directions. Namely,

$$x_o = \left(\frac{\sqrt{12} K_f}{\rho c \dot{\varepsilon}_x} \right)^{2/3}, \tag{59}$$

and,

$$y_o = \left(\frac{\sqrt{12} K_f}{\rho c \dot{\varepsilon}_y} \right)^{2/3}. \tag{60}$$

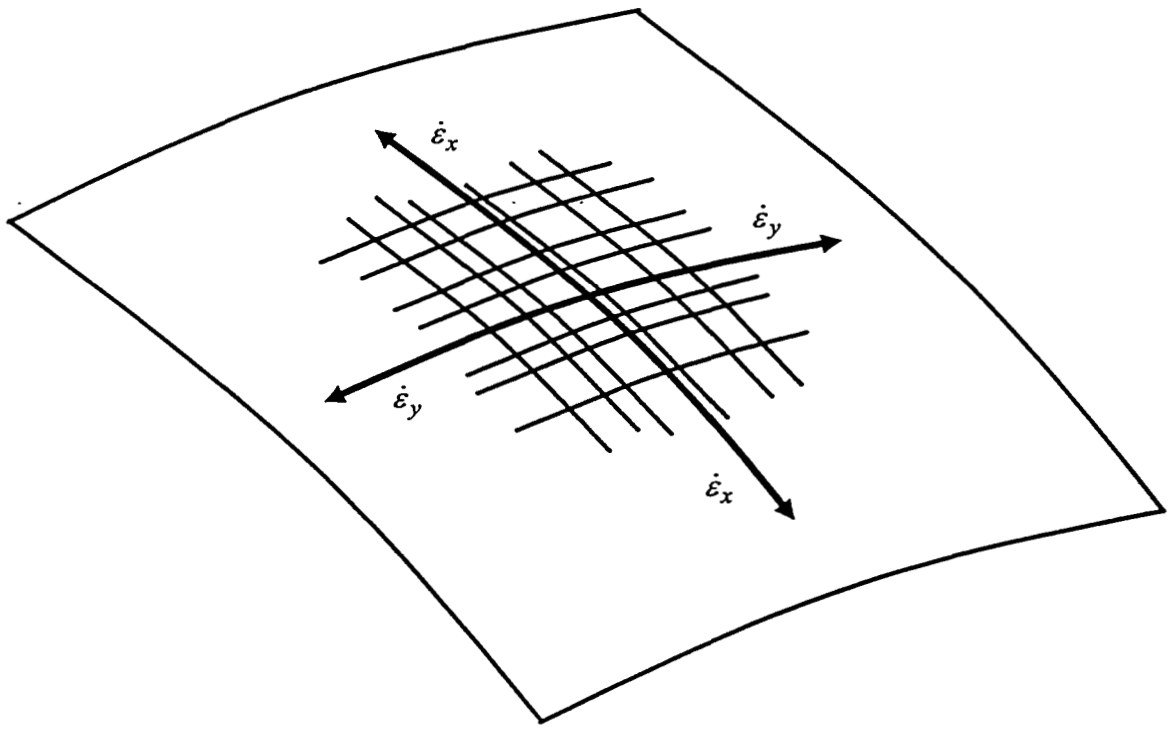

Figure 19. Illustrates independent application of linear statistical fragmentation theory in orthogonal principal stretching directions to implement fragmentation of the surface at a point.

The fragment area scale is then determined from,

$$a_o = x_o y_o = \left(\frac{\sqrt{12} K_f}{\rho c \bar{\dot{\varepsilon}}} \right)^{4/3}, \tag{61}$$

where,

$$\bar{\dot{\varepsilon}} = \sqrt{\dot{\varepsilon}_x \dot{\varepsilon}_y} \, . \tag{62}$$

The nominal fragment aspect ratio is provided by,

$$r_o = x_o / y_o = \left(\dot{\varepsilon}_x / \dot{\varepsilon}_y \right)^{-2/3} . \tag{63}$$

3.3 Application to Biaxial Stretching of U6N

Properties for uranium 6% niobium (U6N) will be used to assess the behavior of the relation for the fragment area scale provided in Equation (61). From the earlier analysis of the uranium ring data of Olsen (2000) a fragmentation toughness of approximately $K_f = 60$ MPa m$^{1/2}$ was determined. This toughness value was also sensibly close to measured static fracture toughness values for U6N. Density and sound speed of $\rho = 17{,}407$ kg/m^3 and $c = 2950$ m/s are those reported by Zurek et al. (2000) for U6N. Based on the present properties for U6N the dependence of the fragment area scale from Equation (61) on the mean stretching rate provided by Equation (62) is shown in Figure 20. At typical stretching rates of a few times 10^3/s up to about 10^4/s for explosively loaded metal shells a fragment size scale on the order of a square centimeter or less is predicted consistent with experimental observation. Increasing strain rate decreases this size scale. Increased toughness, on the other hand, is predicted to increase fragment size.

3.4 Distribution in Fragment Areas

The catastrophic fragmentation of a rapidly stretching metal shell involves a complexity of rapidly opening fissures and cracks that result in a multiplicity of separate fragments. Individual fragments continue on outward divergent paths at the velocity at which breakup occurred. Although the size scale determined previously adequately characterizes the number density and average size of these fragments, a statistical distribution in fragment size is clearly observed. The objective here will be to apply the linear statistical fragmentation theory to characterize the distribution in area fragment size observed experimentally.

In the linear theory, based on the Mott statistical premise, as constrained by the energy-based fracture spacing, a statistical distribution in fracture spacing was determined. The resulting distribution was found to satisfactorily describe linear

fragmentation experiments such as the expanding ring studies. In the present development the assumption of independent statistical fracture in mutually orthogonal principal stretching directions is continued. The statistical size distribution to be pursued is as illustrated in Figure 21. In either the x direction, or in the orthogonal y direction, the statistical spacing of fractures (lines) is governed by the linear Mott statistical distribution with independent length scales of x_o and y_o provided through Equation (61) and Equation (62), respectively. The statistical distribution in spacing in the x direction derived previously (Grady 2001) is,

$$f(x) = \frac{\beta^2}{4}\frac{1}{x_o}\left(\frac{x}{x_o}\right)^3 e^{-\frac{1}{4}(x/x_o)^3}\int_o^1 \left(1-y^2\right)e^{-\frac{3}{4}(x/x_o)^3 y^2}\,dy\ , \tag{64}$$

where $\beta = 3/\Gamma(2/3)$. An equivalent distribution applies to the spacing distribution in the y direction. With further analytic manipulation the integral in Equation (64) can be expressed as an error function if desired.

The linear Mott distribution provided by Equation (64) is not convenient for an analytic determination of the distribution in fragment areas provided by the overlap of horizontal and vertical lines as illustrated in Figure 21. The approach pursued here will be to approximate the distribution from Equation (64) with other analytically tractable distributions. The distributions that will be used are the Weibull distribution,

$$f(x) = \frac{n}{x_o}\left(\frac{x}{x_o}\right)^{n-1} e^{-(x/x)^n}\ , \tag{65}$$

and the gamma distribution,

$$f(x) = \frac{1}{x_o}\frac{n}{\Gamma(n)}\left(\frac{nx}{x_o}\right)^{n-1} e^{-nx/x_o}\ . \tag{66}$$

The Weibull and gamma distributions with the distribution parameter n adjusted to provide the optimum fit are compared with the Mott distribution from Equation (64) in Figure 22. Values for $n = 3.45$ for the Weibull distribution and $n = 8.0$ for the gamma distribution yielded the observed results. The Weibull distribution clearly provides the closer fit to the desired Mott distribution. Both Weibull and gamma distributions will be carried through the analysis developing a fragment area distribution to provide a measure of sensitivity to the fit.

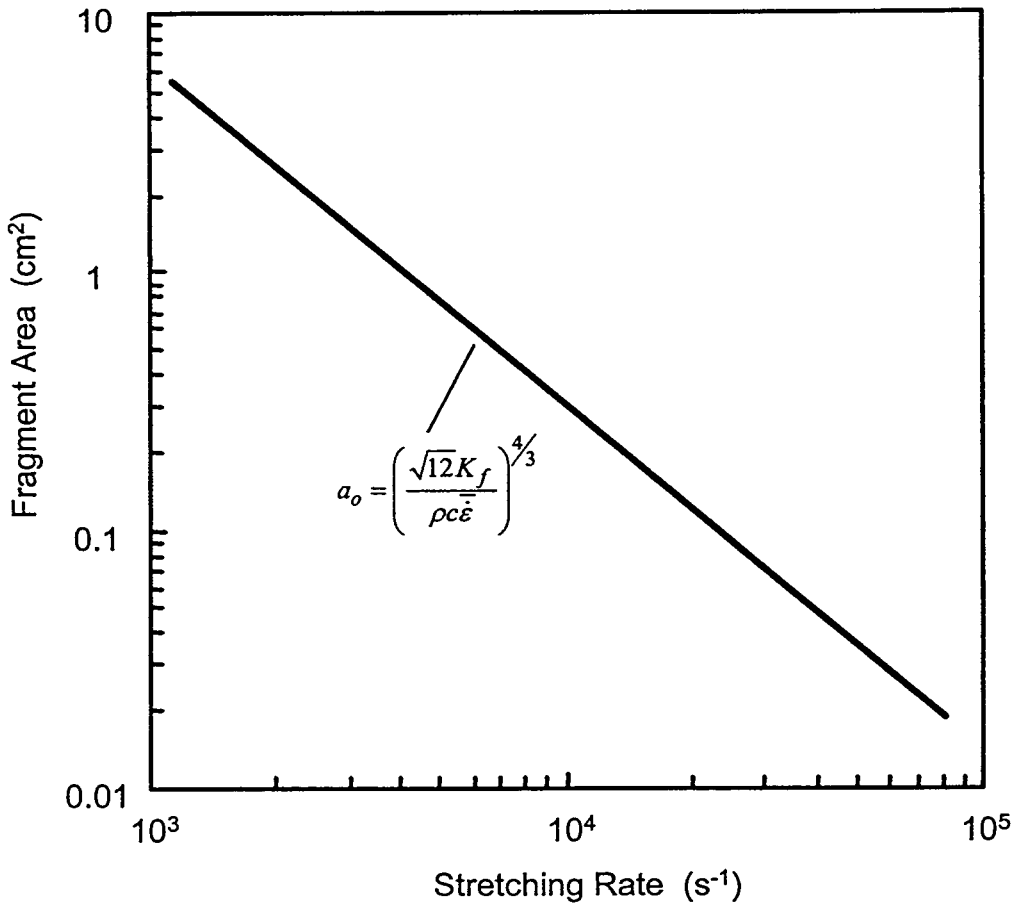

Figure 20. Fragment area scale versus mean stretching rate based on energy determined characteristic fracture spacing and properties for U6N.

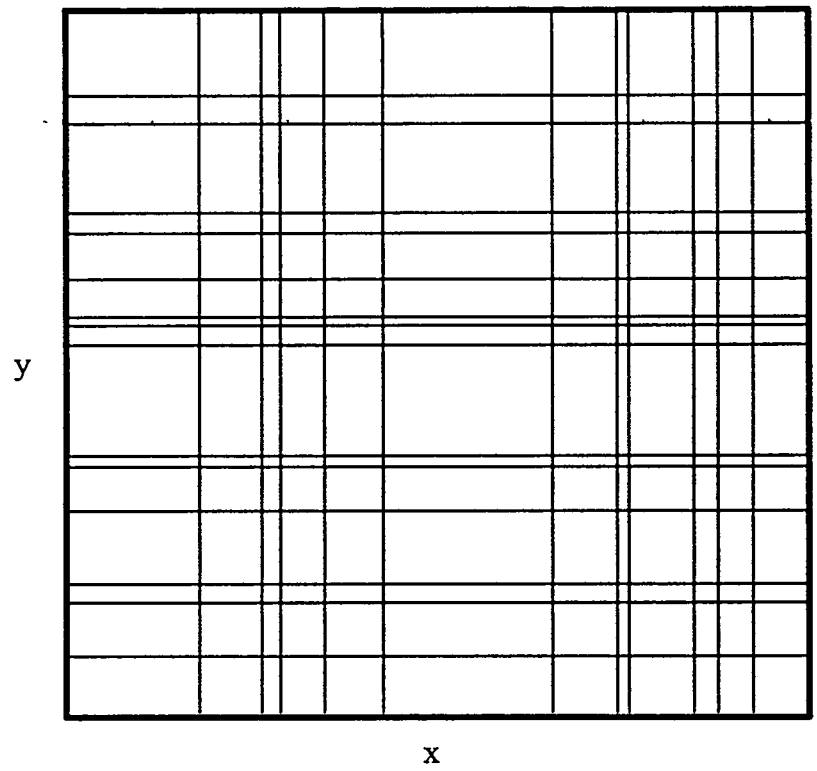

Figure 21. Illustrates independent statistical distributions of fracture spacing in orthogonal *x* and *y* principal stretching directions. Areas determined by intersecting lines will model statistical distribution in fragment areas and fragment aspect rations.

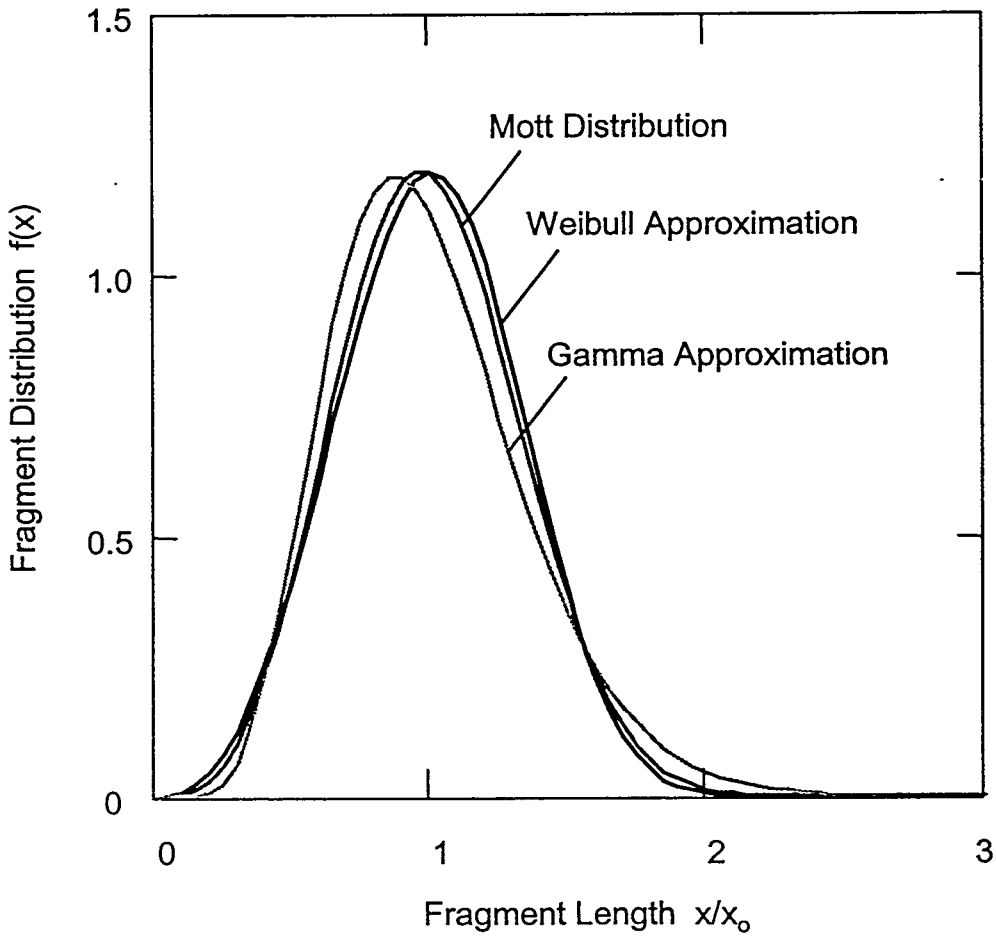

Figure 22. Mott linear fragment size distribution compared with Weibull and Gamma distribution approximations.

Working first with the Weibull distribution, an expression assessing the two-dimensional statistical partitioning of the surface in Figure 21 is immediately written as a juxtaposition of Equation (65) and the corresponding distribution in the y direction.

Namely,

$$f(x,y)=\frac{n^2}{x_o y_o}\left(\frac{xy}{x_o y_o}\right)^{n-1} e^{-(x/x_o)^n} e^{-(y/y_o)^n}, \tag{67}$$

provides the probability density distribution for fragment areas of length x and width y. Equation (67) can be transformed to distribution over fragment area,

$$a = xy, \tag{68}$$

and aspect ratio,

$$r = x/y. \tag{69}$$

The differential invariant,

$$f(x,y)dxdy = g(a,r)dadr, \tag{70}$$

leads to,

$$dxdy = \left|\frac{\partial(x,y)}{\partial(a,r)}\right| dadr, \tag{71}$$

for the differential element through the transformation Jacobian (Buck 1965). Accordingly, the transformed probability density function is,

$$g(a,r) = f\left(x(a,r), y(a,r)\right)\left|\frac{\partial(x,y)}{\partial(a,r)}\right|. \tag{72}$$

Calculating the Jacobian through Equations (68) and (69),

$$\left|\frac{\partial(x,y)}{\partial(a,r)}\right| = \frac{1}{2r}, \tag{73}$$

yields,

$$g(a,r) = \frac{1}{2}\frac{n^2}{(x_o y_o)^n}\frac{a^{n-1}}{r} e^{-\left(\frac{1}{x_o}\sqrt{ar}\right)^n} e^{-\left(\frac{1}{y_o}\sqrt{a/r}\right)^n}. \tag{74}$$

The distribution over fragment area is then written as the integral expression,

$$h(a)=\frac{n^2}{2a_o}\left(\frac{a}{a_o}\right)^{n-1}\int_0^\infty\frac{1}{r}e^{-(\sqrt{a/a_o})^n[(r/r_o)^{n/2}+(r/r_o)^{-n/2}]}dr\,, \tag{75}$$

where $a_o = x_o y_o$ and $r_o = x_o / y_o$.

The substitution,

$$r = r_o e^{2\eta/n}\,, \tag{76}$$

provides,

$$h(a)=\frac{2n}{a_o}\left(\frac{a}{a_o}\right)^{n-1}\int_0^\infty e^{-2(\sqrt{a/a_o})^n\cosh\eta}d\eta\,. \tag{77}$$

The integral is a modified Bessel function (Abramowitz and Stegun 1964) yielding for the area distribution based on a Weibull approximation the area distribution,

$$h(a)=\frac{2}{a_o}\left(\frac{a}{a_o}\right)^{n-1}K_o\left(2\left(\sqrt{a/a_o}\right)^n\right). \tag{78}$$

A similar exercise using the gamma approximation provides,

$$h(a)=\frac{2}{a_o}\left(\frac{n}{\Gamma(n)}\right)^2\left(\frac{n^2 a}{a_o}\right)^{n-1}K_o\left(2n\sqrt{a/a_o}\right). \tag{79}$$

Area distributions resulting from the Weibull and the gamma distribution approximations to the linear Mott statistical fracture spacing distribution are shown in Figure 23. The Weibull approximation provides a noticeably better fit to the linear distribution in Figure 22 and is expected to provide the better representation of the area distribution based on the Mott theory.

Comparison of the Weibull approximation to the Mott area distribution based on random line partitioning of the area is compared with experimental results from the dynamic near-spherical expansion fragmentation of a metal plate in Figure 24. The theoretical distribution reasonably represents the measured experimental distribution.

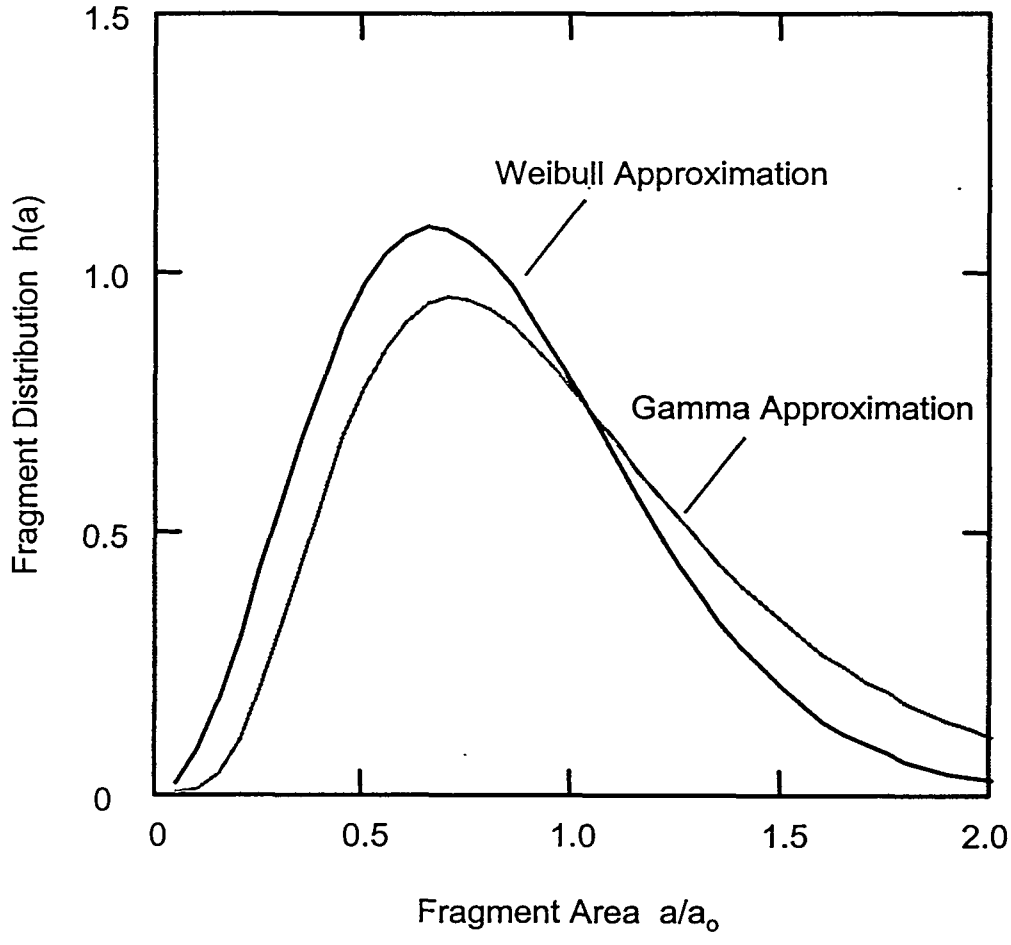

Figure 23. Fragment area distributions based on Weibull and gamma distribution approximations to the Mott linear distribution.

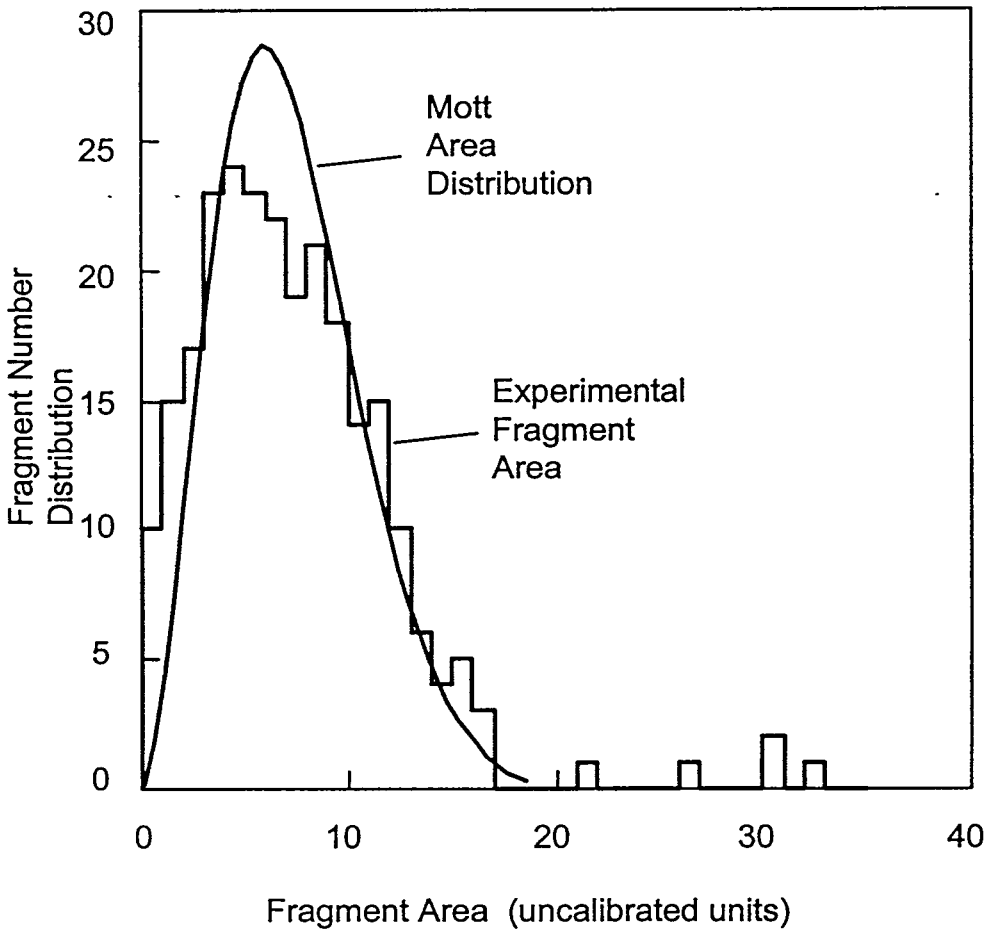

Figure 24. A comparison of the theoretical distribution fragment areas with experimental results.

3.5 Fragment Size Distribution

It is common in the experimental analysis and display of radiographic data of fragmentation of expanding metal surfaces to express the distribution in terms of a characteristic fracture area. For example, we will here identify the fragment size $s=\sqrt{a}$ where a is the previous fragment area defined above. The statistical distribution in fragment size s is a straightforward transformation of the area distributions provided above. For completeness the appropriate statistical size distributions and their pictorial representation will be provided here. The appropriate transformation for Equation (78) based on the Weibull approximation to the linear Mott distribution leads to,

$$h(s)=\frac{4n}{s_o}\left(\frac{s}{s_o}\right)^{2n-1}K_o\left(2(s/s_o)^n\right), \tag{80}$$

for the statistical size distribution. In contrast, Equation (79) based on the gamma approximation provides,

$$h(s)=\frac{4}{s_o}\left(\frac{n^n}{\Gamma(n)}\right)^2\left(\frac{s}{s_o}\right)^{2n-1}K_o\left(2n(s/s_o)\right)\ . \tag{81}$$

Both size distributions are shown and compared in Figure 25.

3.6 Fragment Aspect Ratio Distribution

The analysis pursued here also lends itself to a sensible assessment of the statistical distribution in fragment aspect ratio. Working with the distribution provided by the Weibull representation of the Mott distribution as written in Equation (74), substitute the parameters $r_o=x_o/y_o$, $\xi=a/a_o$ and $\rho=r/r_o$. Integration over the fragment area variable is then written,

$$k(r)=\frac{1}{2}\frac{n^2}{r_o}\frac{1}{\rho}\int_0^\infty \xi^{n-1}e^{-(\rho^{n/2}+\rho^{-n/2})\xi^{n/2}}d\xi\ . \tag{82}$$

Equation (82) is readily integrated providing,

$$k(r)=\frac{n}{r_o}\frac{\rho^{n-1}}{\left(1+\rho^n\right)^2}\ . \tag{83}$$

The distribution over fragment aspect ratio is shown in Figure 26. A similar distribution can be derived for the gamma distribution approximation to the Mott distribution but this development is not done here.

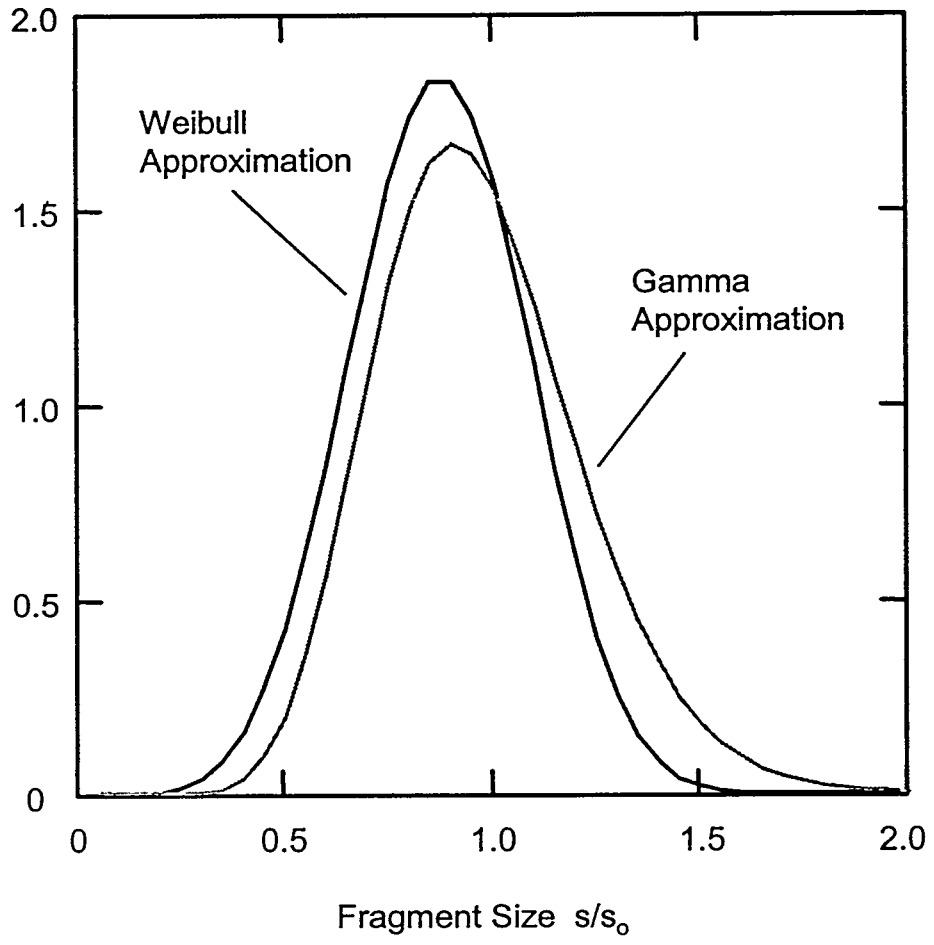

Figure 25. Fragment size distributions based on Weibull and gamma distribution approximations to the Mott linear distribution.

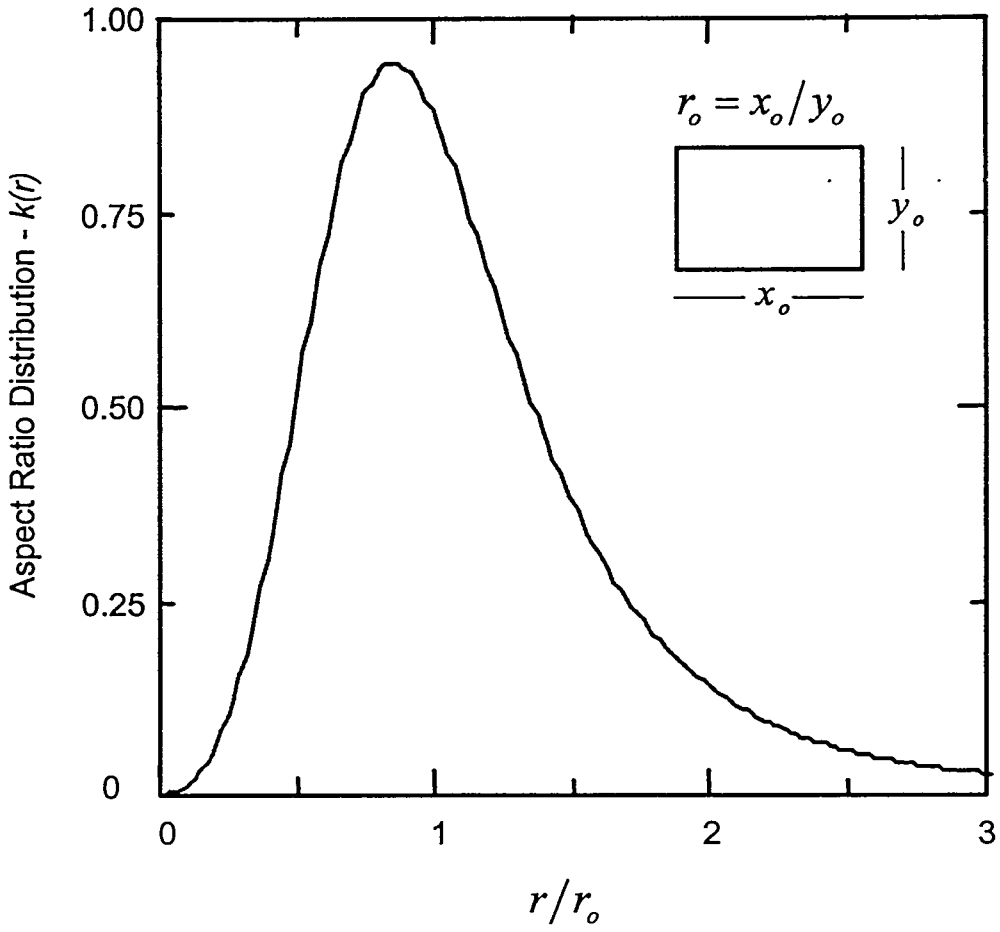

Figure 26. Statistical distribution in fragment aspect ratio.

Section 4 Fracture Criteria

Neither the statistical fragmentation theory of Mott, nor the energy-based theory of fragmentation addresses the underlying deformation that a rapidly expanding metal shell can sustain before onset of fracture. Other physical considerations must be explored in pursuing a theory of the onset of fracture leading to the statistical fragmentation accompanying the disintegration of the expanding shell.

The explosive impulsive loading leads rapidly to the divergent plastic stretching and thinning of the metal shell. The driving explosive pressure quickly diminishes to a negligible level and the outward divergent inertia of the body sustains the plastic deformation. The onset of fracture is dependent on the thermo-plastic deformation properties and the geometry of the metal shell.

Both inertia and strain hardening of the plastic flow affect stability of the expanding and thinning shell. Inertia leads to acceleration stresses which stabilize small perturbations in the thinning process (Romero 1991). Inertial stabilization in this sense, however, does not appear to play a significant role in governing the onset of fracture in the present application.

Deformation hardening in the flow process appears paramount in stabilizing the plastic expansion and is the principal mechanism through which many materials sustain appreciable plastic deformation before rupture. The present dynamic expansion and rupture of metal shells have similarities to the extensive field of quasi-steady metal forming (e.g., Bartlat 1989). The present application can be profitably studied through exploitation of this literature.

In essence plastic strain hardening stabilizes the thinning instabilities brought about by the reduction in in-plane tension caused by thinning of the stretching shell. While strain hardening dominates geometric softening, thinning due to continued stable plastic expansion ensues. Saturation of strain hardening, however, ultimately leads to instability and rupture.

It will be argued that plastic strain hardening and the onset of thinning instability is the dominant mechanism controlling onset of fracture in U6N. An analysis and fracture model based on this load maximum premise is pursued here.

Plastic thinning instabilities are not unique to the dynamic environment. Within the physics introduced, namely rate independent strain hardening and geometric softening, the onset and subsequent growth of thinning instabilities would proceed the same on any time scale from static to rapid dynamic. Additional physical considerations markedly alter the dynamic event, however. These include the properties of material inertia and thermal conductivity in addition to rate sensitivity of the flow properties.

On the length scale of thinning instabilities, plastic dissipation in the dynamic event is effectively adiabatic. Plastic dissipation and the accompanying thermal softening will

alter the effective stress versus strain behavior. Onset of instability would consequently occur earlier than in the corresponding static isothermal event. Adiabatic thermal softening would also localize the thinning instability growth process, markedly changing the character of the thinning and necking region. Unbounded thermal localization in the thinning region is constrained by local inertia, however.

The influence of adiabatic thermal softening on the onset of the tensile thinning instability is expected to be a second order effect. Thermal softening in the subsequent plastic flow during the growth of this instability under the appropriate loading conditions can profoundly alter the failure process, however. Along planes of maximum plastic shear (approximately 45 degrees with respect to the plane of the thinning shell) perturbations in the local temperature or deformation can lead to localized adiabatic shear deformation (adiabatic shear bands) within thin planar regions. Rupture of the expanding shell is then accommodated by the plastic shearing and separation of the body along the planes of adiabatic shear.

Adiabatic shear band failure, like fracture, is enhanced by inhomogeneities in the stress or deformation field. And also like fracture, adiabatic shear bands have a propensity for propagating from a site of initiation through the plane of shear rather than evolving homogeneously throughout that plane. Thus, shear bands depend sensitively on the nature of surface defects which are the dominant source of stress and subsequent deformation inhomogeneity.

Thinning instability and adiabatic shear deformation can cooperate in a more complex serial failure process. Thinning instability can initiate when saturation of plastic strain hardening is overcome by the thinning geometric softening. Adiabatic deformation inhomogeneities brought about during growth of the thinning region can, in turn, trigger local adiabatic shear deformation and complete the failure process.

Plastic thinning instability and localization of adiabatic shear deformation are potential contributions to the processes of failure and rupture of dynamically expanding metal shells. Neither mechanism, however, is either complete, or necessary to the breakup process. Rupture ultimately requires the breaking of molecular bonds and the development of damage within the deforming material. In the fracture of metal this process has been shown to require a level of plastic deformation combined with a state of tensile stress triaxiality. This underlying physics has been noted from at least the early works of Mott and has been addressed in considerable detail by later workers (e.g., Hancock and Mackenzie 1976). This feature of fracture is recognized but will not be pursued in detail in the present development of a failure criterion.

4.1 Biaxial Strain Criterion

A theory and analytic model appropriate to the present dynamic fragmentation application is sought to predict the onset of fracture of a generally biaxial stretching

sheet element of metal as illustrated in Figure 27. Plastic stretching is brought about by an outward expansion velocity V imparted to the body. Current thickness of the element is t while in-plane principal plastic stretching rates are $\dot{\varepsilon}_x$ and $\dot{\varepsilon}_y$, respectively. Equivalent plastic strain in the element is provided through the relation,

$$\dot{\bar{\varepsilon}} = \sqrt{\frac{2}{9}\left[\left(\dot{\varepsilon}_x - \dot{\varepsilon}_y\right)^2 + \left(\dot{\varepsilon}_y - \dot{\varepsilon}_z\right)^2 + \left(\dot{\varepsilon}_z - \dot{\varepsilon}_x\right)^2\right]} \ . \tag{84}$$

Through-the-thickness stretching rate $\dot{\varepsilon}_z$ is related to the current thickness t of the element through the relation $\dot{\varepsilon}_z = \dot{t}/t$. The present problem is adequately addressed by considering motions characterized by the constant proportionality α of the in-plane stretching rates,

$$\alpha = \frac{\dot{\varepsilon}_y}{\dot{\varepsilon}_x} \ . \tag{85}$$

Special cases, of course, include spherical expansion ($\alpha = 1$), uniaxial cylindrical expansion ($\alpha = 0$), and the expanding ring ($\alpha = -1/2$).

Combining Equation (84) and Equation (85) along with the incompressibility condition,

$$\dot{\varepsilon}_x + \dot{\varepsilon}_y + \dot{\varepsilon}_z = 0 \ , \tag{86}$$

yields,

$$\dot{\bar{\varepsilon}} = -\sqrt{\frac{4}{3}\frac{(1+\alpha+\alpha^2)}{(1+\alpha)^2}}\dot{\varepsilon}_z \ . \tag{87}$$

Also, equivalent plastic strain rate is compared with common engineering estimates of the strain rate in Figure 28, illustrating the latter are not appropriate in the present application.

The in-plane, plane stress ($\sigma_z = 0$) effective stress is provided by,

$$\bar{\sigma} = \sqrt{\sigma_x^{\ 2} + \sigma_y^{\ 2} - \sigma_x\sigma_y} \ , \tag{88}$$

where σ_x and σ_y are the in-plane principal stresses. In the present development stresses and strains are thickness averages through the sheet and only in-plane stresses are non-zero. For the corresponding proportional loading to the elastic limit,

$$\sigma_x = E\frac{1+\alpha\nu}{1-\nu^2}\varepsilon_x \ , \tag{89}$$

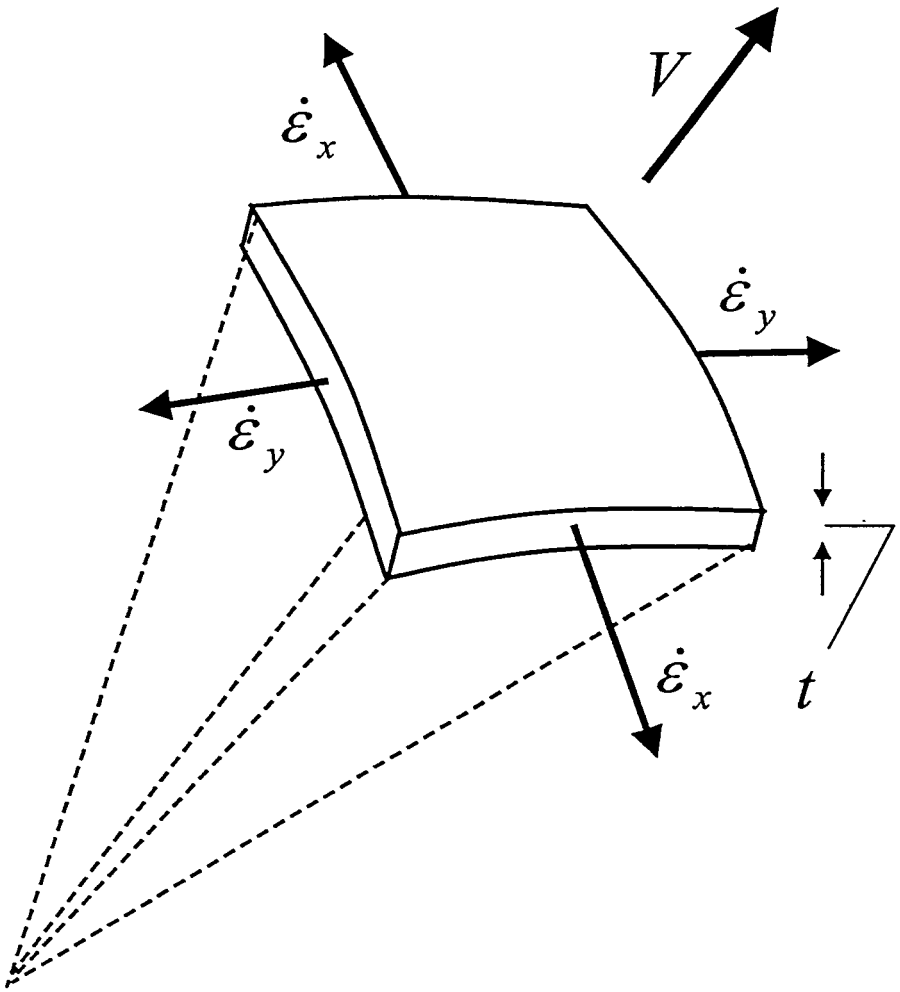

Figure 27. Biaxial expanding element of metal plate with current thickness *t* due to imparted outward velocity *V*. Principal in-plane plastic stretching rates are identified.

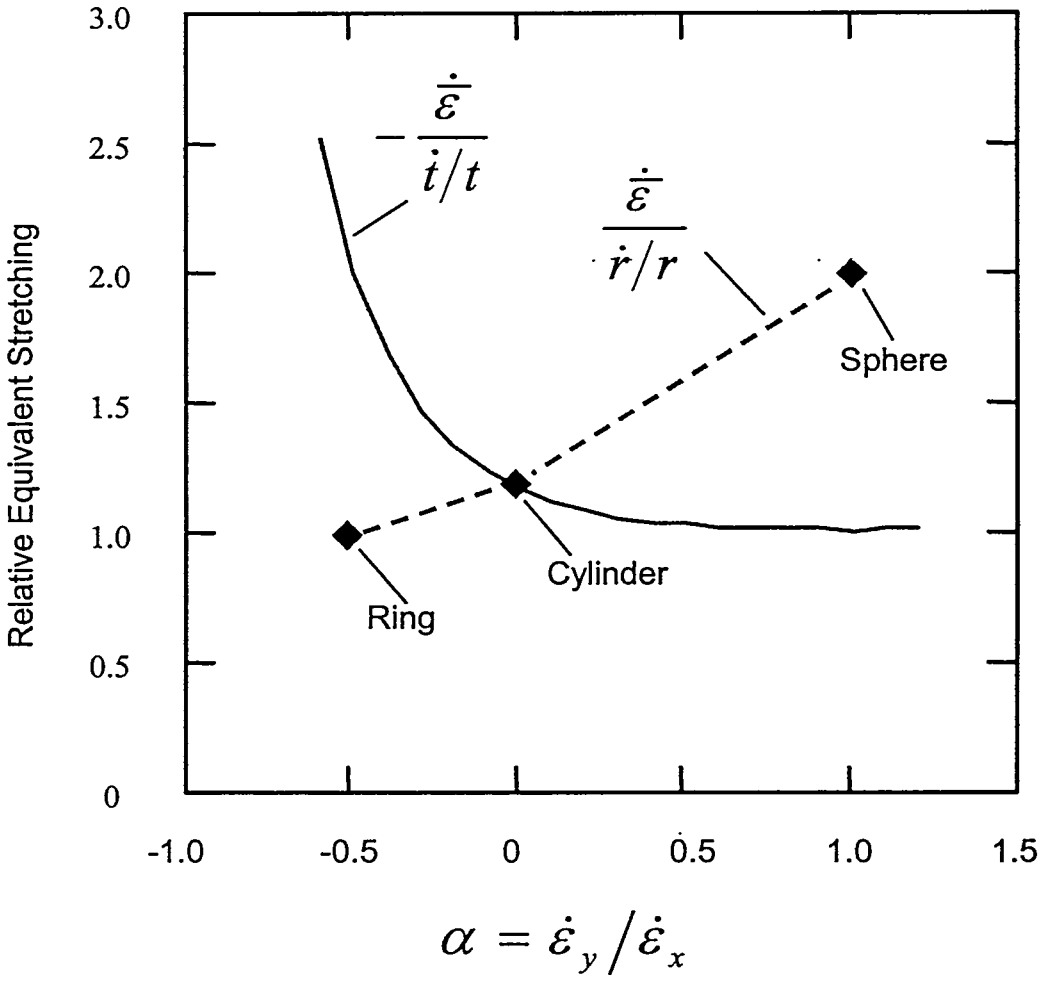

Figure 28. The ratio of equivalent plastic stretching rate to the thinning rate is shown by the solid curve. This ratio relative to the radial expansion rate is also shown for an expanding ring, expanding sphere, and a uniaxial expanding cylinder.

$$\sigma_y = E\frac{\alpha+\nu}{1-\nu^2}\varepsilon_x \ , \tag{90}$$

where E is Young's modulus and ν is Poisson's ratio. The stress ratio is then,

$$\frac{\sigma_y}{\sigma_x} = \frac{\alpha+\nu}{1+\alpha\nu} \ . \tag{91}$$

For a von Mises yield condition,

$$\sigma_x = \frac{Y}{\sqrt{1-\beta+\beta^2}} \ , \tag{92}$$

$$\sigma_y = \frac{\beta Y}{\sqrt{1-\beta+\beta^2}} \ , \tag{93}$$

where Y is the yield stress and β is the stress ratio in Equation (91). Equation (88) for a von Mises material gives $\bar{\sigma} = Y$.

A power-law hardening representation for the adiabatic effective stress versus strain behavior of the material of concern will be assumed of the form,

$$\bar{\sigma} = A\bar{\varepsilon}^n \ , \tag{94}$$

where both the coefficient A and the exponent n may, in general, depend on the biaxial proportionality parameter α. An effective in-plane tension T is provided by the product of the effective stress and the current thickness,

$$T = \bar{\sigma}t = A\bar{\varepsilon}^n t \ . \tag{95}$$

In the present model, onset of fracture is assumed to occur according to the maximum load instability criterion; namely, when the tension $T(\bar{\varepsilon})$ achieves a maximum under the proportional deformation loading. This instability criterion has been found to satisfactorily reproduce results of more detailed stability analyses (e.g., Romero 1991). The maximum of $T(\bar{\varepsilon})$ is identified from the differential,

$$dT = nA\bar{\varepsilon}^{n-1}td\bar{\varepsilon} + A\bar{\varepsilon}^n dt \ . \tag{96}$$

From Equation (87),

$$\bar{\varepsilon} = -f(\alpha)\varepsilon_z \ , \tag{97}$$

where $f(\alpha)$ is identified in the equation and,

$$d\bar{\varepsilon} = -f(\alpha)d\varepsilon_z = -f(\alpha)dt/t \ . \tag{98}$$

Combining Equation (96) and Equation (98) and equating the differential to zero yields for the fracture criterion,

$$\bar{\varepsilon}_f = f(\alpha)n(\alpha) = \sqrt{\frac{4}{3}\frac{(1+\alpha+\alpha^2)}{(1+\alpha)^2}}n(\alpha) \ , \tag{99}$$

where the possible dependence of n on the biaxial proportionality parameter α is noted. Identifying through-the-thickness strain as $\varepsilon_z = \ln t/t_o$,

$$\frac{t_f}{t_o} = e^{-n(\alpha)} \ . \tag{100}$$

For specific geometries of interest zero plastic volume change requires that,

$$r_f t_f^{\kappa(\alpha)} = r_o t_o^{\kappa(\alpha)} \ , \tag{101}$$

where $\kappa(\alpha) = 1/2$, 1, and 2 for an expanding sphere, uniaxial cylinder, and ring, respectively. The radial expansion at failure is then,

$$\frac{r_f}{r_o} = e^{\kappa(\alpha)n(\alpha)} \ . \tag{102}$$

In the absence of further data it is sensible to propose that the power-law hardening coefficient n in Equation (94) be independent of the proportionality parameter α and use the expanding ring data of Olsen (2001) for U6N to establish the coefficient n. The data of Olsen data indicate that $r_f/r_o \cong 1.3$ and Equation (102) provides $n \cong 0.13$.

Through-the-thickness thinning, radial expansion and equivalent strain at fracture for U6N based on the expanding ring data are shown in Figure 29 as a function of biaxiality. The extent of thinning at fracture is independent of biaxiality. Both equivalent strain and radial expansion reduce markedly as biaxiality approaches spherical expansion.

A comment on the load maximum localization criterion is appropriate. It has been noted (e.g., Storen and Rice 1975; Needleman and Tvergaard 1992) that only for $\alpha \leq 0$ is there a line of zero extension determining the orientation of the thinning localization. For $\alpha > 0$ a line of zero extension does not exist. Nonetheless, deformation localization when both in-plane principal strains are positive is observed. Romero (1991) has demonstrated the instability of the Levy-von Mises equations of a biaxially stretching ($\alpha = 1$) perfect plastic plate. The load maximum criterion will be used here to quantify localization onset.

Dependence of the power-law plastic hardening relation in Equation (94) on the strain path α is due, for example, to deformation softening brought about by the growth of micro void damage. The different strain paths imply in turn different states of stress triaxiality. Stress triaxiality equals 1/3 for $\alpha = -1/2$, for example, and equals 2/3 for $\alpha = 1$. Micro void damage growth is known to be a sensitive function of stress triaxiality (e.g., Hancock and Mackenzie 1976).

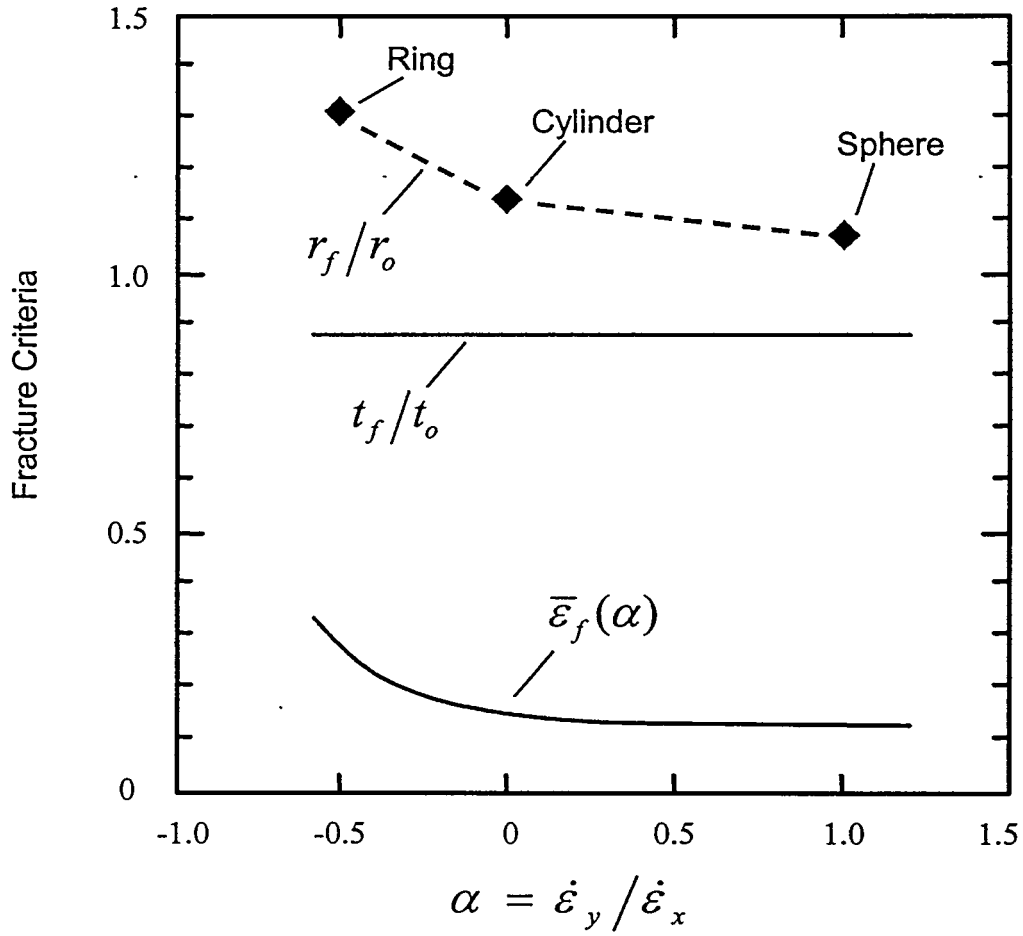

Figure 29. Biaxial fracture equivalent strain, thinning and radial expansion based on expanding ring fracture data of Olsen (2000) on U6N and the Considiere instability criterion.

Nonetheless, load maximum and the concomitant plastic localization is chosen here as the criteria for failure and fracture of the U6N. There is some supporting evidence for this selection. First, the expanding ring data on U6N (Olsen 2001) shows clear evidence of plastic localization preceding fracture. Arrested necking regions are observed in a number of recovered fragments. Extension fracture is observed to occur in necks soon after localization begins. The increase in stress triaxiality within plastic necks is expected to accelerate the fracture process as is observed. Second, the predicted reduced strain to fracture in the range of $0 < \alpha < 1$ (see Figure 29) is also not inconsistent with available data.

Section 5 Analytic Model

A principal objective of the present study is to develop an operational analytic model for the prediction of failure-through-fracture, and the detailed features of the breakup process of an explosively driven metal shell. This operational model is intended to work serially in conjunction with either a computational solution or another operational model, such as the Gurney theory (Grady 2001), which accounts for the explosive loading and acceleration of the metal shell. The operational fracture and fragmentation model is an uncoupled post-processing model in the sense that no aspect of the model feeds back to the loading and acceleration solution. Output from the explosive loading and acceleration solution, on the other hand, provides crucial input to the fracture failure and fragmentation model.

Application of the model will be focused here principally on problems mimicking, in the language of Gurney, the open-faced sandwich or the closed sandwich geometries. The former involves a relatively modest thickness of explosive (perhaps a few centimeters) in intimate contact with the thin metal shell. The latter geometry considers two thin shells of metal which encloses the explosive. The shells will be curvilinear in construction such that an inner and outer shell will be apparent. These two geometries differ from a spherical or closed-cylinder metal shell fully loaded with explosive in that the duration of explosive shock and high-pressure loading will be quite short compared to the closed shell geometries. The model is certainly expected to be applicable to the latter geometries. It is believed, however, that the modes of fracture failure in the fully loaded shell will be quite different from the present sandwich geometries of interest.

Detonation of the explosive leads to shock loading and outward acceleration of the metal shell. (For the closed sandwich geometry, the inner shell will be concurrently driven inward. Failure and breakup of the outer shell is of principal interest.) Detonation of the explosive is commonly initiated at a specific point or points in the geometry and loading throughout most of the metal shell occurs through a sweeping obliquely-incident detonation wave. Peak pressures in the shock wave initially coupled into the metal can range over approximately 30–60 GPa. Outward acceleration to velocities in the kilometer per second range is rapid, occurring over a few microseconds. Outward motion of the metal shell is divergent due to the curvilinear geometry of the shell and explosive resulting in plastic thinning of the shell. Driving pressures also drop promptly due to the rapid expansion and decompression of the explosive products. The explosive shock loading and acceleration is calculated in detail through computational simulations of the event. In Gurney solutions momentum and energy balance determine the imparted motions (Grady 2001).

There are concerns that initial explosive shock loading leads to marked metallurgical changes of the shell metal which must be accounted for in the failure and fragmentation process. This possible effect has not yet been fully demonstrated but is

not of consequence to the model developed here. Material properties relevant to the shocked material can be entered into the model if needed.

In principle, metal shells of interest will have complex geometries ranging from primarily cylindrical curvilinearity in certain regions to near spherical curvilinearity in others. Thickness variations may also be present. Obstructions or barriers to the motion of the shell can locally restrict flow causing gradients in the kinetics imparted by the explosive.

Consequently, the operational model determining fracture failure and fragmentation applies at a point on the shell and application of the model requires a determination at a predetermined grid of points or, at a minimum, at points of specific concern.

Failure through fracture in the model is governed by the cumulated equivalent plastic strain identified in the previous section. Although a measure of equivalent plastic strain modulated by the stress triaxiality (the ratio of the mean stress to the equivalent shear stress) could certainly be implemented into the model, this complication will not be included here except in the simplest sense. During the initial shock compression and acceleration a plastic strain of the order of ten percent is incurred. This plastic strain is assumed to not contribute to either microscopic fracture damage or to the deformation hardening saturation leading to thinning localization. This assumed feature of the model is readily implemented by discounting equivalent plastic strain accumulated when stress triaxiality is negative. (The convention with mean pressure negative in compression is assumed.)

Ignoring the plastic strain generated during the strong shock and release process is not done here without a certain level of discomfort. It is difficult to imagine that the shock-induced strain does not contribute to some extent to the deformation hardening, the saturation of which leads ultimately to load maximum and localization. Nonetheless, load maximum localization is sensibly consistent with the available failure data on U6N and will be used in this development as the fracture failure criteria. As noted previously, features of the fragmentation model do not depend on the form of the failure criteria. An improved failure model could be readily implemented at a later time if warranted.

Therefore, fracture failure at a computational point of the explosively loaded metal shell is provided by Equation (99). The material function $n(\alpha)$ appropriate to U6N is applied. The kinematic solution, either through a Gurney calculation, or from a numerical simulation, must provide the history of the equivalent strain and the ratio α of the principal in-plane stretching rates.

MathCAD programs developed based on both the Gurney theory and the computational simulation of the explosive loading are provided in the appendix.

5.1 The Gurney Model

In the Gurney model development the analysis focuses on a curvilinear metal shell element of an explosive-metal system with cylindrical symmetry about an axis of revolution. Metal shell and explosive thicknesses and densities are entered. A Gurney velocity characterizing the explosive energy is also entered and the appropriate Gurney equation (Grady 2001) is used to calculate the imparted expansion velocity to the element assumed normal to the shell element surface.

An initial polar and azimuthal arc radius, $r_{\pi o}$ and $r_{\phi o}$, respectively, are input and, with the calculated expansion velocity, used to calculate in-plane strains and strain rates in the polar and azimuthal directions. Based on the load maximum failure parameter $n(\alpha)$ the time after launch of the shell element is advanced until the equivalent strain failure criteria is satisfied. The time and displacement at failure, along with strains and strain rates, are then output and stored for further calculations.

Metal density, sound speed, and fragmentation toughness are entered and used to calculate the characteristic fracture spacing in the polar and azimuthal directions. Average fragment area, fragment size, and distribution properties are then calculated.

Lastly, features of crack-opening at a specified time after fracture are determined, including the total crack-opening crack area and statistical features of the widths of cracks.

5.2 The Post-Processing Model

The post-processing model considers a region of a cylindrically symmetric curvilinear metal shell in which the motion of the shell is specified by other means. These means could include a computational simulation of the explosive-metal event in which motions of the region of the shell of concern are determined from the position and velocity histories of tracer points selectively positioned in the metal shell.

For the example included in the appendix, realistic analytic relations to describe the shell geometry and motions are used rather than a computer simulation. Within the shell element of interest the position and velocity history of three points lying on an in-plane polar ray are determined. The azimuthal strain and strain rate at the central point is readily calculated from the radial position and velocity at this point. Polar strain and strain rate are approximated from the motion through the separation and rate of separation of the tracer points.

Failure of the element and the subsequent fragmentation and crack-opening displacement features are calculated in the same way as in the Gurney model.

5.3 Comparison with Fragmentation Experiments

Experiments have recently been performed at the Sandia National Laboratories Impact Facilities which offer an opportunity for testing the present preliminary engineering model. In these experiments a tube of U6N metal several inches long, with initial O.D. =0.75" and I.D. = 0.50", was subjected to an internal radial impulsive loading through the impact of stationary and high velocity plastic cylinders near the tube center. Rapid radial expansion with a central radial velocity of approximately 200–250 m/s led to dynamic fracture and fragmentation near the central region of the tube. Three images of the tube at successive stages through the fragmentation process shown in Figure 30 illustrate the failure behavior.

The present rather cursory comparison worked within the framework of the post-processing model—an example of which is provided in the appendix. The initial elliptical geometry provided in the model was used to approximate a tube by making the z axis adequately long. Diameter of the initial ellipse was selected as the average from the tube I. D. and O. D. A radial expansion velocity of 250 m/s was used. The radial velocity profile was changed from the functional form provided in the example in the appendix to better describe the finite radial bulging seen in the high-speed photography (Figure 30). In particular, the radial velocity was varied quadradically from 250 m/s at the center to zero at an axial distance of 10 mm. Standard properties for U6N as described in this text were otherwise maintained.

Calculation of fragmentation was performed at a point 5 mm from the tube centerline. Failure was predicted to occur at 5.6 μs after start of initial motion with a radial displacement of 1.03 mm. This prediction is fully consistent with the high-speed photography in which striations indicative of fracture initiation are observed at a center-line radial expansion of about 2.0–2.5 mm.

Predicted strain rates at onset of fragmentation are 2.0×10^4/s in the azimuthal direction and 3.6×10^3/s in the polar direction. Corresponding azimuthal and polar fracture spacings are calculated to be 3.3 and 11.0 mm, respectively. Comparisons with the middle and lower photographs in Figure 30 show the predictions are in sensible accord with the test.

Lastly, the final photograph in Figure 30 occurs approximately 20 μs after fracture onset. At this time the post-process model calculates a crack opening area fraction of 34% with an average azimuthal crack opening width of 2.1 mm and a statistical range over about 1.0 to 3.2 mm. Crack opening predictions are also reasonably borne out by the late-time photograph in Figure 30.

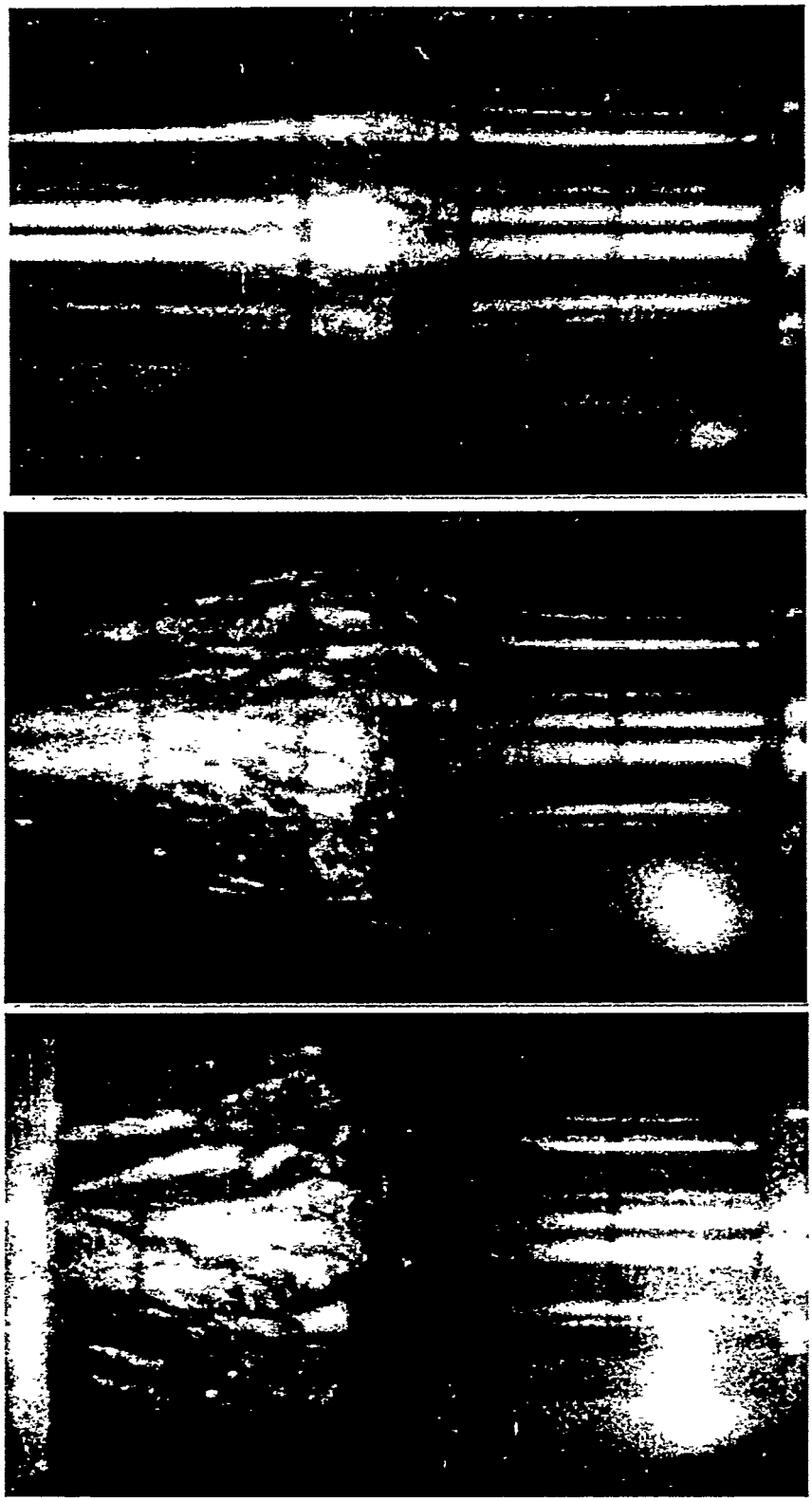

Figure 30. Selected images of SNL U6N tube fragmentation test DU-2.

Section 6 Discussion and Conclusions

During the current report period key features regarding the physics and statistics of dynamic fragmentation, within the scope of the approaches pursued initially by Mott and later by the present author, have fallen nicely into place. The largely statistical ideas of Mott, and the later energy-based concepts, are shown here to be sensibly compatible.

Based on very reasonable assumptions this fragmentation theory is extended to the general dynamic breakup of an expanding metal shell. The fragmentation theory is joined with a physical model for the prediction of the amount of expansion strain the shell can accommodate before onset of fracture. With the joining of the theories quite general calculations regarding the statistical temporal and spatial breakup of the shell can be made.

Preliminary engineering codes have been pursued to exercise the failure and fragmentation models. Demonstration calculations with these codes have been performed.

Continued efforts need to focus in further detail on some of the key fracture and fragmentation phenomena essential to the underlying model physics. This addition study will be nicely driven by new experimental methods that are being pursued.

Also, additional development and verification of the engineering codes will be needed. This effort will also benefit from emerging experimental results.

Section 7 References

Abramowitz, M. and I. A. Stegun, eds. 1964. *Handbook of Mathematical Function.* No. 55. National Bureau of Standards Applied Mathematics Series, U. S. Government Printing Office.

Barenblatt. 1962. *Adv. Appl. Mech.* 7: 55.

Barker, L.M. and R. E. Hollenbach. 1972. Velocity interferometer for measuring the velocity of any reflecting surface. *J. Appl. Phys.* 43: 4669–4680.

Barlat, F. 1989. *Forming Limit Diagrams – Predictions Based on Some Microstructural Aspects of Materials, in Form Limit Diagrams: Concepts, Methods and Applications.* Edited by R. H. Wagner, K. S. Chang, S. P. Keeler. The Minerals, Metals & Materials Society.

Buck, R. C. 1965. *Advanced Calculus.* New York: McGraw-Hill.

Dugdale 1960. *J. Mech. Phys. Solids.* 8: 100.

Grady, D. E. 1981. Fragmentation of Solids Under Impulse Stress Loading, *J. Geophys. Res.* 86: 1047–1054.

Grady, D.E. 1982. Local inertia effects in dynamic fragmentation. *J. Appl. Phys.* 68: 322–325.

Grady, D. E., M. E. Kipp and D. Benson. 1984. Energy and statistical effects in the dynamic fragmentation of metal rings. Chapter 2 in *Mechanical Properties at High Rates of Strain.* Edited by J. Harding. Bristol: Inst. Physics.

Grady, D.E. 1993. Dissipation in Adiabatic Shear Bands. *Mechanics of Materials.* 17: 289–293

Grady, D. E. 2001. Investigation of Explosive Driven Fragmentation of Metals. Progress Report I, Applied Research Associates Technical Report, April.

Getis, A. and P. H, Jackson. 1971. The Expected Proportion of a Region Polluted by k Sources. *Geographical Analysis.* 3: 256–261.

Hahn, G. J. and S. S. Shapiro. 1967. Statistical Models in Engineering. New York: John Wiley & Sons.

Hancock, J. W., and A. C. Mackenzie.1976. On the Mechanisms of Ductile Failure in High-Strength Steels Subjected to Multi-Axial Stress States. *J. Mech. Phys. Solids.* 24: 147–169.

Johnson, W. A. and R. F. Mehl. 1939. Reaction Kinetics in Processes of Nucleation and Growth, Trans. *AIMME*. 135: 414–458.

Kipp, M. E. and D. E. Grady. 1985. Dynamic fracture growth and interaction in one dimension.. *J. Phys. Mech. Solids*. 33: 399–415.

Kipp, M. E., and D.E. Grady. 1986. Random Flaw Nucleation and Interaction in One Dimension. In *Metallurgical Applications of Shock-Wave and High-Strain-Rate Phenomena*. Edited by L.E. Murr, K.P. Staudhammer, and M.A. Meyers. Marcel Dekker, Inc.

Mott, N. F. 1943. Fragmentation of H. E. Shells: A Theoretical Formula for the Distribution of Weights of Fragments. Ministry of Supply, AC3642, March.

Mott, N. F. 1943b. A theory of the fragmentation of shells and bombs. Ministry of Supply AC4035, May.

Mott, N. F. 1947. Fragmentation of shell cases. *Proc. Royal Soc.* A189, 300–308, January.

Olsen, M. L. 2001. Private Communication.

Needlemann, A., and V. Tvergaard. 1992. Analyses of Plastic Flow Localization in Metals. *Applied Mechanics Reviews*. 45: S3–S18.

Romero, L. A. 1991. The Stability of Stretching and Accelerating Plastic Sheets I &II. *J. Appl. Phys.* 69: 7474–7499.

Storen, S., and J. R. Rice. 1975. Localized Necking in Thin Sheets. *J. Mech. Phys. Solids.* 23: 421–441.

Zurek, A. K., R. S.Hixson, W. W. Anderson, J. E. Vorthman, G. T. Gray, and D. L. Tonks. 2000. Spall Response of U-Nb (6%) Alloy. In DYMAT 2000, Sixth International Conference on Mechanical and Physical Behaviour of Materials Under Dynamic Loading, Krakow, Poland, September 25-29, EDP Sciences, 677–682.

Section 8 Appendix

The present appendix includes the MathCAD equations and examples for the engineering fragmentation models based on Gurney theory explosive loading concepts and on post-processing of a computational simulation of the explosive loading event.

Gurney Model
for
Failure and Fragmentation
of a
Curvilinear Shell Element

I. Gurney Solution

Calculation of the velocity V_b of the exterior plate M_b. Planar open sandwich geometry is assumed. Explosive C_b in front of the stationary radius is first calculated. Then the velocity V through Gurney equation.

Inputs:

Explosive and metal densities and thicknesses plus Gurney Velocity V_G = SQRT (2E).

$\rho_a := 15000 \qquad t_a := 4 \cdot 10^{-3}$

$\rho_b := 17407 \qquad t_b := 6 \cdot 10^{-3}$

$\rho_c := 1600 \qquad t_c := 40 \cdot 10^{-3}$

$V_G := 1300$

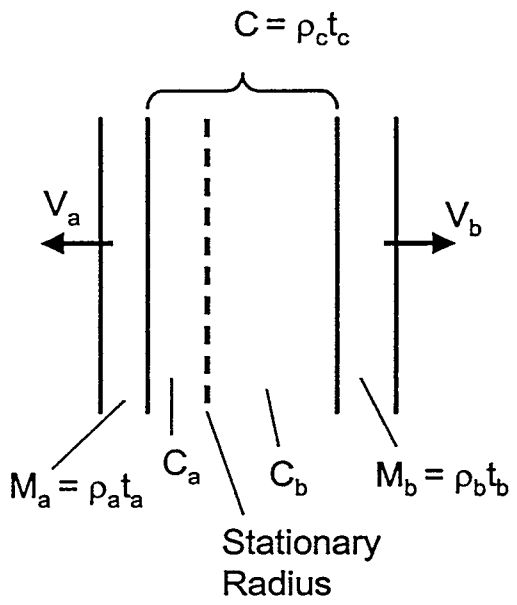

Calculations:

$M_a := \rho_a \cdot t_a$

$M_b := \rho_b \cdot t_b$

$C := \rho_c \cdot t_c$

$$C_b := \frac{C}{2} \cdot \left(\frac{C + 2 \cdot M_a}{C + M_a + M_b} \right)$$

$$T_b := \frac{C_b}{C}$$

$$V_L := \frac{V_G}{\left(\frac{M_b}{C_b} + \frac{1}{3} \right)^{0.5}}$$

Solutions:

The launch velocity V_L of plate b while T_b is relative thickness of explosive driving plate b.

$V_L = 620.777 \qquad T_b = 0.403$

II. Strain-to-Failure Solution

Failure of the expanding surface element is calulated through a load maximum criterion. Strain, strain rate, strain biaxiality, element displacement and failure time are calculated.

Inputs:

Load maximum failure parameter n(α). A more complex model could include triaxiality parameter throuqh a dependence of n(α) on α.

$$n_\alpha := 0.13$$

Element launch velocity: Either input a velocity or accept velocity calculated in Model Section I.

$$V_L = 620.777$$

Divergent flow of the outward accelerated is determined by:

Polar Arc Radius $(r_{\pi o}, r_\pi)$ Azimuthal Arc Radius $(r_{\phi o}, r_\phi)$

$$r_{\pi o} := 0.20 \qquad r_{\phi o} := 0.15$$

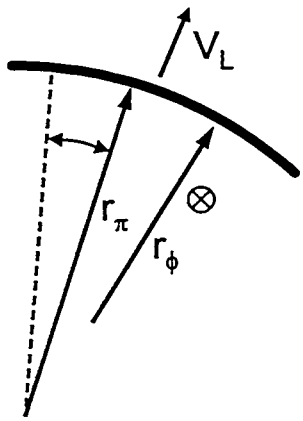

Thinning gradient parameters. This part of model contributes to the polar straining.

Time after launch.

$$t := 19 \cdot 10^{-6}$$

Calculations:

Increment time-after-launch until failure achieved (F = 1).

$$r_\pi := r_{\pi o} + V_L \cdot t \qquad r_\phi := r_{\phi o} + V_L \cdot t \qquad d_L := V_L \cdot t$$

$$\varepsilon_\pi := \ln\left(\frac{r_\pi}{r_{\pi o}}\right) \qquad \varepsilon'_\pi := \frac{V_L}{r_\pi} \qquad \varepsilon_\phi := \ln\left(\frac{r_\phi}{r_{\phi o}}\right) \qquad \varepsilon'_\phi := \frac{V_L}{r_\phi}$$

$$F := \varepsilon_\pi + \varepsilon_\phi \geq n_\alpha \qquad \alpha := \frac{\varepsilon'_\pi}{\varepsilon'_\phi} \qquad t_L := t$$

Solutions:

Failure corresponds to F = 1 while T_L and D_L are the corresponding time and displacement.

$$F = 1 \qquad t_L = 19 \times 10^{-6} \qquad d_L = 0.012$$

Strain, strain rate and strain biaxiality at failure.

$$\varepsilon_\pi = 0.057 \qquad \varepsilon_\phi = 0.076 \qquad \varepsilon'_\pi = 2.931 \times 10^3 \qquad \varepsilon'_\phi = 3.837 \times 10^3 \qquad \alpha = 0.764$$

III. Fragment Size and Spacing

Size and statistics of fragmentation at failure in surface element based on energy (fracture toughness) criterion for fracture spacing. Provides average polar and azimuthal fracture spacing, fragment average surface area and aspect ration and distribution.

Inputs:

Fragmentation Toughness (K_f) for shell metal. Also density (note density from Section I = ρ_b) and sound speed of metal are inputs to fracture spacing length scale.

$K_f := 60 \cdot 10^6$ $\rho_m := \rho_b$ $c_{lm} := 2950$

Calculations:

$$x_\pi := \left(\frac{\sqrt{12} \cdot K_f}{\rho_m \cdot c_{lm} \cdot \varepsilon'_\pi} \right)^{\frac{2}{3}} \qquad x_\phi := \left(\frac{\sqrt{12} \cdot K_f}{\rho_m \cdot c_{lm} \cdot \varepsilon'_\phi} \right)^{\frac{2}{3}}$$

$a_o := x_\pi \cdot x_\phi$ $a_{0.05} := 0.41 \cdot a_o$ $a_{0.95} := 1.68 \cdot a_o$

$x_{av} := \sqrt{a_o}$ $x_{0.05} := \sqrt{a_{0.05}}$ $x_{0.95} := \sqrt{a_{0.95}}$ $r_o := \frac{x_\phi}{x_\pi}$

Solutions

Polar and azimuthal spacing.

$x_\pi = 0.012$ $x_\phi = 0.010$

Fragment area size scale and, 5% and 95% area cut-off.

$a_o = 128.509 \times 10^{-6}$

$a_{0.05} = 52.689 \times 10^{-6}$

$a_{0.95} = 215.895 \times 10^{-6}$

Characteristic fragment size and, 5% and 95% area cut-off.

$x_{av} = 0.011$

$x_{0.05} = 0.007$

$x_{0.95} = 0.015$

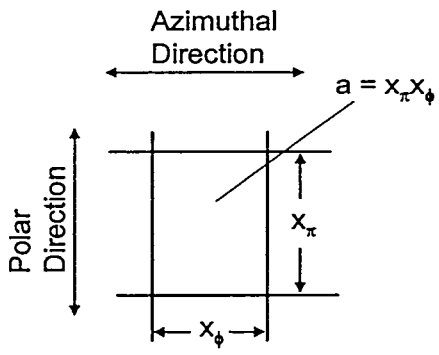

IV. Crack Opening Displacement

Failure and continued expansion leads to continued opening of fractures and fizzures. Calculations are provided for the fraction of open area and the size and distribution of crack width as a function of time after failure.

Inputs:

Time from explosive launch to failure is calculated above. Input time after failure here.

$$t_f := 10 \cdot 10^{-6}$$

Calculations:

Fractions of crack opening in polar and azimuthal directions are calculated at time t_f:

$$f_\pi := \frac{\varepsilon'_\pi \cdot t_f}{1 + \varepsilon'_\pi \cdot t_f} \qquad f_\phi := \frac{\varepsilon'_\phi \cdot t_f}{1 + \varepsilon'_\phi \cdot t_f}$$

Which provides fraction of crack opening area at time t_f.

$$f_{\pi\phi}(t_f) := f_\pi + f_\phi - f_\pi \cdot f_\phi$$

The mean gap opening in at time t_f in polar and azimuthal directions along with 5% and 95% distribution limits is provided through:

$$w_{\pi ave} := 1.47 x_\pi \cdot \varepsilon'_\pi \cdot t_f \qquad w_{\phi ave} := 1.47 x_\phi \cdot \varepsilon'_\phi \cdot t_f$$

$$w_{\pi 0.05} := 0.72 x_\pi \cdot \varepsilon'_\pi \cdot t_f \qquad w_{\phi 0.05} := 0.72 x_\phi \cdot \varepsilon'_\phi \cdot t_f$$

$$w_{\pi 0.95} := 2.29 x_\pi \cdot \varepsilon'_\pi \cdot t_f \qquad w_{\phi 0.95} := 2.29 x_\phi \cdot \varepsilon'_\phi \cdot t_f$$

Solutions:

Crack opening area fraction and corresponding time after failure and after launch.

$$f_{\pi\phi}(t_f) = 0.064 \qquad t_f = 10.0 \times 10^{-6} \qquad t_L + t_f = 29.0 \times 10^{-6}$$

Gap size and distribution characteristics.

$$w_{\pi ave} = 534.3 \times 10^{-6} \qquad w_{\phi ave} = 584.5 \times 10^{-6}$$

$$w_{\pi 0.05} = 261.7 \times 10^{-6} \qquad w_{\phi 0.05} = 286.3 \times 10^{-6}$$

$$w_{\pi 0.95} = 832.4 \times 10^{-6} \qquad w_{\phi 0.95} = 910.5 \times 10^{-6}$$

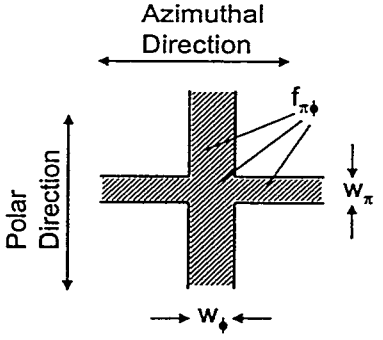

Post-Processing Model for Failure and Fragmentation of an Explosive Driven Curvilinear Metal Shell

I. Motion of Element

The metal shell is assumed to be an ellipse of revolution about the z axis. An analytic velocity history is assigned to all points on the shell. The solution provides the position and velocity history of a point and two neighboring points for the purpose of estimating the asimuthal and polar in-plane stretching rates

Inputs:

Parameters for the geometry and velocity history of the metal shell are input.

$a_o := .15 \quad b_o := .30 \quad V_a := 1400 \; V_b := 1400 \quad \tau := 3 \cdot 10^{-6}$

The point of the shell of interest and polar distance to right and left neighboring points are input.

$z_p := .15 \quad \delta_p := .01 \quad n := 1,2..3$

$z_o(n) := z_p + (n-2) \cdot \delta_p$

$r_o(n) := a_o \cdot \left[1 - \left(\frac{z_o(n)}{b_o} \right)^2 \right]^{0.5}$

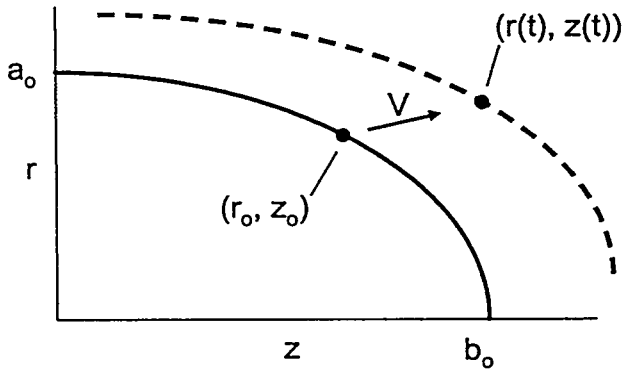

The time step and number of time steps are input.

$m := 0,1..20 \quad \delta t := 1 \cdot 10^{-6}$

$t(m) := m \cdot \delta t$

Calculations:

Position and velocity of element points (n) at all time steps (m) are calculated for point p(m,n).

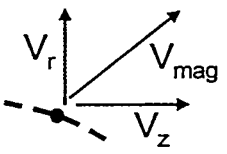

$V_z(m,n) := z_o(n) \cdot \frac{V_b}{b_o} \cdot \left(1 - e^{\frac{-t(m)}{\tau}} \right) \qquad V_r(m,n) := r_o(n) \cdot \frac{V_a}{a_o} \cdot \left(1 - e^{\frac{-t(m)}{\tau}} \right)$

$V_{mag}(m,n) := \left(V_z(m,n)^2 + V_r(m,n)^2 \right)^{0.5}$

$z(m,n) := z_o(n) \cdot \left[1 + \frac{V_b}{b_o} \cdot \left[t(m) - \tau \cdot \left(1 - e^{\frac{-t(m)}{\tau}} \right) \right] \right]$

$r(m,n) := r_o(n) \cdot \left[1 + \frac{V_a}{a_o} \cdot \left[t(m) - \tau \cdot \left(1 - e^{\frac{-t(m)}{\tau}} \right) \right] \right]$

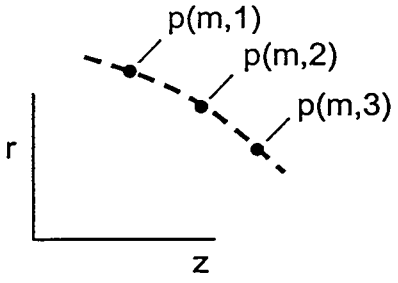

Increment time-after-launch until failure achieved (F = 1). Then calculate strain biaxiality, and time and displacement to failure.

$$F := \varepsilon_\pi + \varepsilon_\phi \geq n_\alpha \qquad \alpha := \frac{\varepsilon'_\pi}{\varepsilon'_\phi} \qquad t_L := t(m) \qquad d_L := \sqrt{\left(r(m,2) - r_o(2)\right)^2 + \left(z(m,2) - z_o(2)\right)^2}$$

Solutions:

Failure corresponds to F = 1.

$$F = 1$$

t_L and d_L are the corresponding time and displacement.

$$t_L = 13 \times 10^{-6} \qquad d_L = 0.014$$

Polar and azimuthal strain, strain rate and strain biaxiality at failure.

$$\varepsilon_\pi = 0.049 \qquad \varepsilon_\phi = 0.09 \qquad \varepsilon'_\phi = 8.422 \times 10^3 \qquad \varepsilon'_\pi = 4.736 \times 10^3$$

$$\alpha = 0.562$$

III. Fragment Size and Spacing

Size and statistics of fragmentation at failure in surface element based on energy (fracture toughness) criterion for fracture spacing. Provides average polar and azimuthal fracture spacing, fragment average surface area and aspect ration and distribution.

Inputs:

Fragmentation toughness (K_f) for shell metal. Also density and sound speed of metal are inputs to fracture spacing length scale.

$K_f := 60 \cdot 10^6$ $\rho_m := 17407$ $c_{lm} := 2950$

Calculations:

$$x_\pi := \left(\frac{\sqrt{12} \cdot K_f}{\rho_m \cdot c_{lm} \cdot \varepsilon'_\pi} \right)^{\frac{2}{3}} \qquad x_\phi := \left(\frac{\sqrt{12} \cdot K_f}{\rho_m \cdot c_{lm} \cdot \varepsilon'_\phi} \right)^{\frac{2}{3}}$$

$a_o := x_\pi \cdot x_\phi$ $a_{0.05} := 0.41 \cdot a_o$ $a_{0.95} := 1.68 \cdot a_o$

$x_{av} := \sqrt{a_o}$ $x_{0.05} := \sqrt{a_{0.05}}$ $x_{0.95} := \sqrt{a_{0.95}}$ $r_o := \frac{x_\phi}{x_\pi}$

Solutions

Polar and azimuthal spacing.

$x_\pi = 9.006 \times 10^{-3}$ $x_\phi = 6.136 \times 10^{-3}$

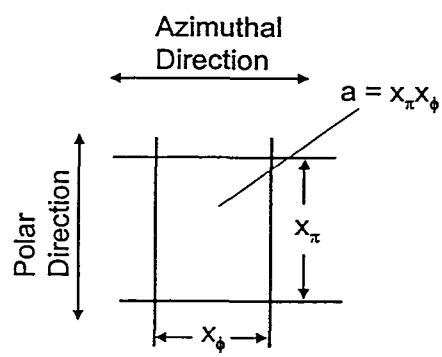

Fragment area size scale and, 5% and 95% area cut-off.

$a_o = 55.258 \times 10^{-6}$ $a_{0.05} = 22.656 \times 10^{-6}$ $a_{0.95} = 92.834 \times 10^{-6}$

Characteristic fragment size and, 5% and 95% area cut-off.

$x_{av} = 7.434 \times 10^{-3}$ $x_{0.05} = 4.76 \times 10^{-3}$ $x_{0.95} = 9.635 \times 10^{-3}$

IV. Crack Opening Displacement

Failure and continued expansion leads to continued opening of fractures and fizzures. Calculations are provided for the fraction of open area and the size and distribution of crack width as a function of time after failure.

Inputs:

Time from explosive launch to failure is calculated above. Input time after failure here.

$$t_f := 10 \cdot 10^{-6}$$

Calculations:

Fractions of gap opening in polar and azimuthal directions are calculated at time t_f:

$$f_\pi := \frac{\varepsilon'_\pi \cdot t_f}{1 + \varepsilon'_\pi \cdot t_f} \qquad f_\phi := \frac{\varepsilon'_\phi \cdot t_f}{1 + \varepsilon'_\phi \cdot t_f}$$

Which provides fraction of gap area at time t_f.

$$f_{\pi\phi}(t_f) := f_\pi + f_\phi - f_\pi \cdot f_\phi$$

The mean crack opening opening in at time t_f in polar and azimuthal directions along with 5% and 95% distribution limits is provided through:

$$w_{\pi ave} := 1.47 x_\pi \cdot \varepsilon'_\pi \cdot t_f \qquad w_{\phi ave} := 1.47 x_\phi \cdot \varepsilon'_\phi \cdot t_f$$

$$w_{\pi 0.05} := 0.72 x_\pi \cdot \varepsilon'_\pi \cdot t_f \qquad w_{\phi 0.05} := 0.72 x_\phi \cdot \varepsilon'_\phi \cdot t_f$$

$$w_{\pi 0.95} := 2.29 x_\pi \cdot \varepsilon'_\pi \cdot t_f \qquad w_{\phi 0.95} := 2.29 x_\phi \cdot \varepsilon'_\phi \cdot t_f$$

Solutions:

Crack opening area fraction and corresponding time after failure and after launch.

$$f_{\pi\phi}(t_f) = 0.119 \qquad t_f = 10.0 \times 10^{-6} \qquad t_L + t_f = 23.0 \times 10^{-6}$$

Crack opening size and distribution characteristics.

$$w_{\pi ave} = 627 \times 10^{-6} \qquad w_{\phi ave} = 759.6 \times 10^{-6}$$

$$w_{\pi 0.05} = 307.1 \times 10^{-6} \qquad w_{\phi 0.05} = 372 \times 10^{-6}$$

$$w_{\pi 0.95} = 976.7 \times 10^{-6} \qquad w_{\phi 0.95} = 1.2 \times 10^{-3}$$